ONLINE DETERMINATION OF EXTRACELLULAR GLUTATHIONE IN ORGANOTYPIC HIPPOCAMPAL SLICE CULTURES WITH A MCIROFLUIDIC DEVICE AND CONFOCAL LASER-INDUCED FLUORESCENCE DETECTION SYSTEM

by

Juanfang Wu

B.S., Tongji University, P.R. China, 2003

M.S., Tsinghua University, 2006

Submitted to the Graduate Faculty of

School of Arts and Sciences in partial fulfillment

of the requirements for the degree of

Master of Science

University of Pittsburgh

2010

UNIVERSITY OF PITTSBURGH

SCHOOL OF ARTS AND SCIENCES

This thesis was presented

by

Juanfang Wu

It was defended on

September 9th, 2008

and approved by

Adrian Michael, Professor, Department of Chemistry

David Pratt, Professor, Department of Chemistry

Thesis Director: Stephen G Weber, Professor, Department of Chemistry

Online determination of extracellular glutathione in organotypic hippocampal slice cultures with a microfluidic device and confocal laser-induced fluorescence detection system

Juanfang Wu, M.S.

University of Pittsburgh, 2010

GSH is an essential cellular antioxidant in the brain cells due to its active sulfhydryl group. Measuring the concentration, distribution and metabolic pathways of GSH and related compounds provides a lot of useful information for studying oxidative insult in vivo. Microfluidic chips are ideal platforms for biological samples, because they are capable of analyzing very small amount of analyte in a relative short time. The coupling of microfluidic separation and laser-induced fluorescence provides an effective way for analyzing GSH and related compounds.

A confocal LIF detection system has been developed in our laboratory. The key part in building this system is the selection of an optimized set of optical components, which mainly includes a laser, an objective, a front surface mirror, lens, filter sets and a detector. The parameters of these optical components were first optimized according to the preliminary scheme of the system. Meanwhile, an opto-mechanical assembly was designed and made for arranging these components into a whole system. A controlling program in LabVIEW was also developed, which incorporates several major functions, such as data collection and pretreatment, voltage and current monitoring, high voltage power supply (HVPS) manipulation, sampling control, into one program and offers an easy access for user to have a convenient control of the whole system.

The procedures of beam alignment for our detection system are discussed in detail in the system testing section. The profiles of the focused laser beam at three different positions were measured by using a simple setup, the results of which were consistent with those from the theoretical calculation. A series of experiments were designed to identify the dominant noise sources in the system for a better signal to noise ratio (SNR). Noise reduction was finally obtained by applying averaging and low pass filter. Experiments with real samples showed that the linear range for GSH labeled with Thioglo 1 is between 0-49.7 μM and the limit of detection (LOD) is around 1.45 nM for our system.

Our future work will be focused on connecting electroosmotic sampling with separation on microfluidic device to analyze the extracellular GSH in organotypic hipocampal slice cultures.

TABLE OF CONTENTS

LIST OF TABLES

LIST OF FIGURES

PREFACE

I would like to thank my advisor, Prof. Stephen G. Weber. It is a great pleasure to have chance to work with him. He offered me great chance to carry out the interesting projects and patiently guided and encouraged me whenever I met difficulties or problems in research.

I would like to thank Dr. Jerome Ferrance in University of Virginia. Although I have not met him face to face, he gave me a lot of useful and important suggestions about the design of the detection system and microfluidic devices through email.

I would like to express my gratitude to my committee membranes, Prof. Adrian Michael and Prof. Shigeru Amemiya for their kind assistance during my comprehensive exam.

I am also thankful to Weber group for their helpful suggestions and continuous encouragement in my research work.

I would like to thank electronic shop and Machine shop for their help and patience.

In addition, I would like to thank National Institute of Health for generous financial support.

1.0 INTRODUCTION

Reduced glutathione (GSH, L-γ-glutamyl-L-cysteinylglycine) is a ubiquitous tripeptide composed of glutamic acid, cysteine and glycine (Figure 1). It is widely distributed in all mammalian tissues with a concentration normally ranging from 0.1 to 10 mM, which is much higher than that of other compounds with the same sulfhydryl group like cysteine and cystine.[1] GSH lacks the toxicity associated with free cysteine, which enables itself to be a suitable candidate molecule to maintain a certain thiol/disulfide redox potential.[2] Due to its active sulfhydryl group, GSH plays a key role in the defense of cells against oxidative stresses, which are resulted either from external sources like the onset of inflammatory process, the exposure to UV radiation or oxidative chemicals or from internal source like the generation of reactive oxygen species (ROS) through various metabolic pathways.[3]

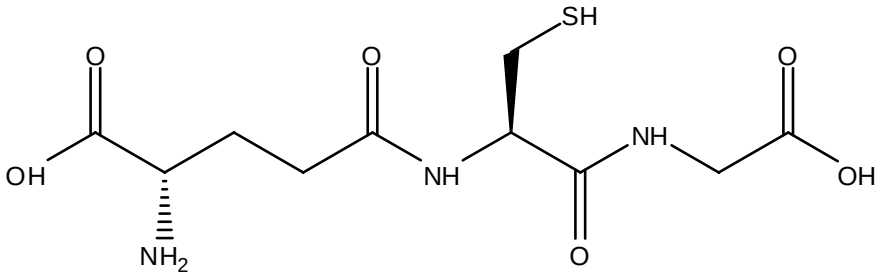

Figure 1. GSH structure

The cells in human brain utilize 20% of the oxygen consumed by the body although they constitute only 2% of the body weight.[4] This fact implies that ROS might be generated at high

rates within the brain and thus the brain must have some effective mechanisms in dealing with this potential risk of ROS to maintain healthy functions. Excessive ROS will lead to DNA strand breaks, lipid peroxidation and protein modification and finally the loss of neurons during the neurological diseases in the brain, *e.g.*, Parkinson's disease, Alzheimer's disease, Huntington's disease and stroke.[5] Numerous studies have proved that GSH is an essential cellular antioxidant in the brain cells.[5-7]

Because of their unique functions, the concentration, distribution and metabolic pathways of GSH and related compounds become a useful tool for studying the oxidative insult in biological samples. Various biochemical assays and analytical methods have been developed to determine the GSH and its related precursors or metabolites in biologic matrices.[2, 3] The analytical methods involved can be divided into two main categories, non-separative and separative. Non-separative methods have advantages in its simplicity; however they are often limited by the unsatisfactory specificity and selectivity. The most common techniques that appear in recent published papers are spectrophotometric assay,[8] spectrofluorimetric assay,[9] amperometry[10, 11] and electro-spin resonance,[12] etc. High-performance liquid chromatography (HPLC) and capillary electrophoresis (CE) are the most popular separative methods. Besides, other more common techniques also find their applications in researches related with GSH, such as thin-layer chromatograph (TLC),[12] gas chromatography (GC)[13-15] and microfluidic chip.[13, 16-19]

Although sensitivity is not a critical issue for determination of GSH and related compounds in the intracellular space, it is important when the concentration GSH is significant lowered by the chemical or physical agents or when GSH in the extracellular space is of interest.[3] The microfluidic chip is an ideal platform for biological samples, because it is capable of analyzing very small amount of samples in a relatively short time.[20-22] Meanwhile, it is very

convenient to etch micro components with different functions onto one chip and to connect other analytical techniques like microdialysis to realize on-line separation and detection.[23-25] Laser-induced fluorescence (LIF) is the most generally used detection method in microfluidic separation.[26-28] The high spatial coherence of the laser source permits the excitation of small sample volumes with high efficiency, which enables them to be the most sensitive techniques for detection following chemical separation. The coupling of microfluidic separation and LIF enhances their advantages and provides an effective way for analyzing GSH and related compounds.

1.1 PATHWAYS AND FUNCTIONS OF GSH IN BRAIN

1.1.1 Pathways of GSH

The homeostasis for GSH is maintained in brain both by recycling of glutathione constituents within the brain and by transferring other precursors such as glutamine and cysteine from blood across the blood-brain barrier.[7] The synthesis of GSH in brain cells is similar to that in other tissues. There two enzymes involved consecutively in this process, γGlutamylycysteine (γGluCys) synthetase and GSH synthetase (Figure 2).[7, 29] With the presence of γGluCys synthetase, glutamate and cysteine firstly form the dipeptide, γGluCys, which further reacts with glycine to form GSH by the catalysis of GSH synthetase. Both steps are adenosine triphosphate (ATP) consuming steps. A feedback inhibition of γGluCys synthetase is realized by the concentration of the end product GSH.[30]

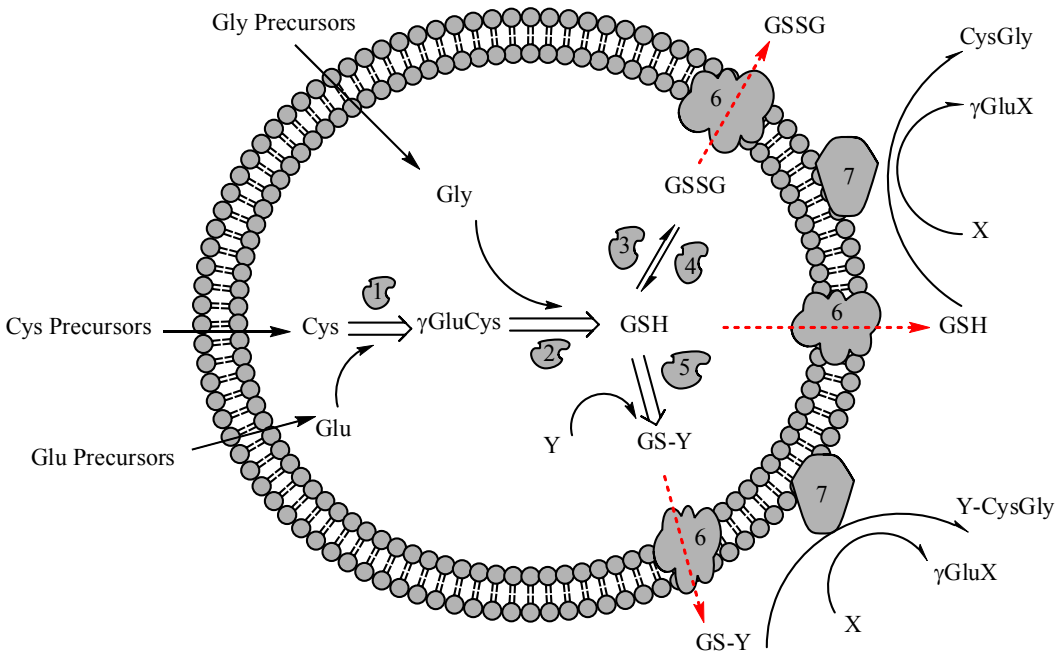

Figure 2. Metabolism of glutathiones in cells [5, 7]

X represents an acceptor of the γ-glutamyl moiety transferred by γ-glutamyl transpeptidase from glutathione. Y is a substate of glutathione-S-transferase(s). 1, γ-glutamylcysteine synthetase; 2, glutathione synthetase; 3, glutathione peroxidase(s); 4, glutathione reductase; 5, glutathione-S-transferase(s); 6, Mrps/MRPs; 7, γ-glutamyl transpeptidase.

Different types of brain cells may use different precursors to synthesize GSH in the intracellular compartment. Astrocytes (also known as astroglial cells) and neurons are the two cell types in which the metabolism of GSH has been widely studied,[6, 31-33] The cytosolic glutathione concentration of astroglial cultures is about 8 mM, which is higher than that in neurons. This cell type prefers to use glutamate and cystine as extracellular GSH precursors,[34] however, neurons can only use extracellular cysteine as precursor instead of cystine.[35] The best extracellular precursor for the glutamate moiety is glutamine.[36] There is an intensive metabolic exchange between astroglial cells and neurons (Figure 3). GSH released from astroglial cells becomes the substrate for the astroglial ectoenzyme γ-glutamyl transpeptidase (γGT), which

produces cysteinylglycine (CysGly). This molecule will then serve as a precursor of neuronal GSH. GSH synthesis in neurons strongly depends on the cysteine provided by the neighboring astrocytes.[5, 7] At the cellular level, astroglial cells play a key role in the defense of the brain against ROS. It also support other brain cells types in this respect.[37]

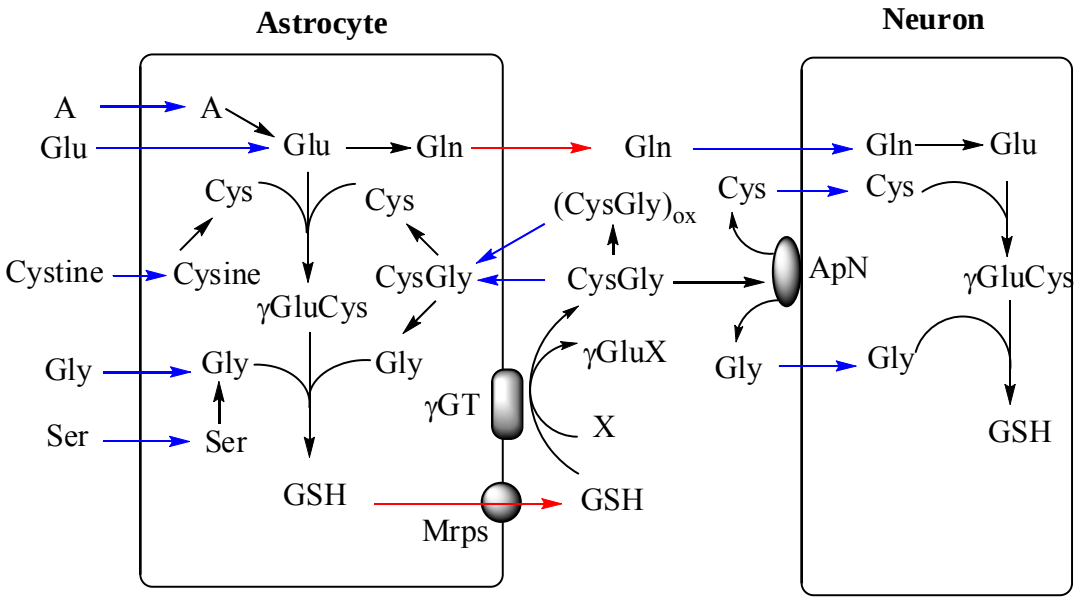

Figure 3. Metabolic interaction between astrocytes and neurons in glutathione metabolism.[5, 7] A represents amino acids which are metabolized by astrocytes to generate glutamate. X represents an acceptor of the γ-glutamyl moiety transferred by γGT from glutathione

During the detoxification of ROS, GSH is able to react with radicals directly or to react with peroxides with the help of glutathione peroxidase (GPx).[5, 6] The product of these processes is glutathione disulfide (GSSG). Under the catalysis of glutathione reductase (GR), GSSG is converted back into GSH intracellularly, which is accompanied by the oxidation of NADPH to $NADP^+$ (Figure 4). There are other possible pathways for lowering the intercellular concentration of GSH. One of these pathways is related with glutathione S-transferases (GSTs). GSTs belong

to a family of phase Ⅱ detoxification enzymes and the main function of these enzymes is to conjugate the electrophilic xenobiotics to the endogenous nucleophile GSH to form less toxic and more hydrophilic products, which can be partically metabolized and excreted from the cells.[38-40] These conjugates are also the substrates for γGT to CysGly conjugates.[5, 6] Finally, GSH may also be released by some certain types of cells to the extracellular compartment.[41-47] The proteins which is in charge of the export of GSH, GSSG and glutathione S-conjugates are members of multidrug resistance proteins (MRPs for human transporters; Mrps for the transporters of other species).[5]

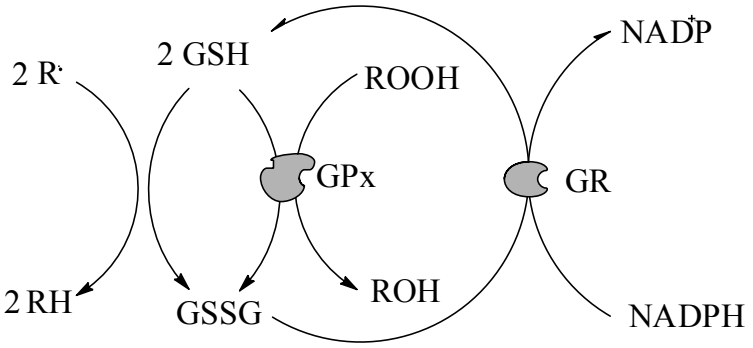

Figure 4. GSH pathway in the detoxification of ROS[6]

GSH reacts with radical (R•) directly and GSH reacts with peroxides (ROOH) catalyzed by GPx. The regeneration of GSH is achieved by glutathione reductase(GR) and cofactor NADPH.

Release of GSH from brain cells has been reported mainly for astrocytes.[5, 43] These cells release under unstressed conditions GSH and not GSSG.[43, 48, 49] This phenomenon was initially underestimated due to the existence of the ectoenzyme γGT.[5] Normally, astrogial cells export about 10% of their intracellular GSH per hour.[50] The half life of the astroglial cells GSH is about 5 h according to the experimental results.[51] This efflux process follows apparent Michaelis-Menton kinetics with the K_m value of 36 mM.[43] On the contrary, an effective release of GSSG

during oxidative stress has been reported as a mechanism of cellular self-defense.[52] The K_m value for this process is about 93 μM.[53] Intracellular concentration of GSH is a main factor that affects the rate of GSH release.[43] Compared to astrocytes, neurons, microgial cells and oligodendrocytes only excrete marginal amount of GSH.[48]

1.1.2 Functions of GSH

GSH has a series of biological functions and the deficiency in GSH redox cycle will lead to a number of diseases in human.[5, 7, 54-56] Compared with other organs, brain is especially vulnerable to ROS because it is rich in lipid with unsaturated fatty acids.[1] GSH is well-known for its role as an antioxidant.[57-59] It can react with varieties of ROS directly or with the help of enzyme.[6] It interacts closely with other antioxidants in the body, such as ascorbate and α-tocopherol to form a firm cellular defense system against ROS.[46, 57, 60, 61] GSH is also active in detoxification of xenobiotics.[1, 62] It is a cofactor in isomerization reactions and a safe form of storing and transporting cysteine.[7, 29, 62] In addition, it is related with the regulation of cell proliferation,[63-65] apoptosis[2, 64, 66, 67] and maintains the thiol redox potential in cells.[63, 68]

The concentration of extracellular GSH in brain is in the low micro molar range, which is much lower than that in the intracellular space, meanwhile, the concentration of GSH was found elevated during ischemia.[69, 70] There are some other special functions of extracellular glutathione in the brain. Firstly, it serves as key factor in the metabolism interaction between astroglial cells and neurons as mentioned above. Secondary, GSH is considered to be a neurohormone based on some special characteristics found in the researches.[71-74] For example, the extracellular existence of GSH in brain; a release of glutathione from brain slices upon stimulation; the presence of specific extracellular receptors for GSH; the stimulation of a signal cascade in astrocytes and the

induction of sodium currents in neocortex.[7] Thirdly, it serves as an antidote for toxic compounds such as glutamate through the reaction under the catalysis of γGT to form γ-glutamyl glutamate.[41, 44, 69] GSH and its product may also act as an agonist and modulators of glutamate receptors in brain.[75, 76] Other studies also indicate that GSH and its related enzymes might be also involved in the leukotriene metabolism, which has neuroendocrine and excitatory functions in brain.[7] Last but not least, GSH released to extracellular space may contribute to the maintenance of the GSH level in the cerebrospinal fluid.[77] Nevertheless, elevated extracellular concentration of GSH may also increase the neuronal vulnerability to hypoxia and glucose deprivation and to enhance excitotoxicity.[78, 79] From this point of view, obtaining a homeostasis of GSH in both intracellular and extracellular spaces is vital for a sound metabolism system.

1.2 DETERMINATIONS OF GSH AND RELATED METABOLITES

1.2.1 Sample pretreatment

There are several forms of glutathione existing in biological substrates, which increases the complexity of the analysis.[1] GSH and its disulphide form GSSG constitute the free glutathione fraction. The total glutathione usually refers to the summation of the free glutathione and the protein-bounded GSH. Under suitable conditions, one form of GSH is able to change to other forms, which always leads to the erroneous estimation and misinterpretation of the results. Besides, most of the methods used to analyze GSH are based on its characteristic thiol group, other aminothiols in bio-samples may also interfere with the quantification of GSH and related compounds. Oxidation and proteolysis are two major factors which lead to transformation of one

form of GSH to another.[3] At pH values greater than 7, GSH undergoes rapid auto-oxidization to form GSSG. Meanwhile, γGT reaches its optimum activity at neutral pH, which catalyzes the first step of GSH proteolysis. In order to prevent introducing human error into the analysis system and truly reflect the concentrations and distribution of the GSH and related compounds in the original sample, it is of vital importance to select proper conditions during the sample pretreatment. Firstly, it is wise to keep the pH value of the buffer below 7 and maintain the sample in refrigeration to minimize the autoxidation and enzymatical proteolysis of the GSH. Secondary, it is helpful to precipitate the proteins from the sample by acidification using trichloroacetic acid, trifluoroacetic acid, metaphosphoric acid, perchloric acid, or 5-sulfosalicylic acid and then centrifuge it to minimize proteolysis. Besides, removal of protein will also improve the performance in the later analytical procedure like sample injection and separation in HPLC or in CE. Thirdly, special attentions should be paid to procedures like sonication, which may cause the cell lysis. As the concentration in the intracellular space is usually much higher than that in the extracellular space, mixing the GSH from these two different sources will lead to the distortion of the GSH levels in both compartments. Moreover, it has also been suggested to add redox quenching buffers composed of HCl, ascorbic acid and diethylenetriaminepentaacetic acid into the system to restrain thiol oxidation.[80] Other reagents such as N-ethylmaleimide (NEM), iodoacetic acid, or 2-vinyl pyridine are often used to block the thiol group and to prevent the oxidation of GSH.[81] Inhibitors of γGT and chelating agents of ferrous ions like 1,10 phenanthroline or EDTA have also been used to prevent proteolysis and oxidative reactions to a certain extent.[82]

Sample collection is the main step in the pretreatment. Different specimens may have their special requirements. The most common bio-specimens involved in the GSH assay are cells,

subcellular organelles, whole blood, plasma and serum, tissue, and even a partial of a specific organ in vivo, etc. Erythrocytes are the most common cells included in the GSH assay. They are normally obtained by centrifuging the whole blood with proper conditions, such as 5,000 g for 10 min at 4 ºC, to separate the red cell pellet from the plasma. After removal the upper layer of plasma, cold distilled water could be added into the remaining erythrocytes to disrupt it. The lysate could then be stored at -80 ºC for further analysis.[13] However, if the single cell analysis is to be performed, the lysis step could be achieved right before or after cells are introduced into the analysis system.[83-86] Procedures for preparing plasma from the blood sample is similar to those described for erythrocytes, except that the plasma portion is collect and store for further use.[81, 87] For subcellular organelles like mitochondria, further steps like repeated centrifugation (10000 g for 10 min at 4 ºC) and resuspension are required to enrich the mitochondrial fraction from cells.[88, 89] When the matrix related with tissue, there are usually several choices for sample collection. If the total GSH in the tissue is of interest, the sample could first be homogenized and diluted in EDTA buffer. The resultant solution is then sonicated for a short time depending on the kind of tissue, say 10 s for vitreous sample from eye tissue. The mixture is further treated with centrifugation and the supernatant is eligible for storage and analysis.[90] The incubation medium is also an informative source for monitoring the efflux of GSH from slice cultures to the extracellular space. The incubation medium of the slice can be collected at a certain interval and concentration of analytes can be determined after the separation and detection.[44, 91] Microdialysis is a good choice for sampling extracellular GSH in vivo with relative good spatial resolution and small damage to tissue. A typical concentric microdialysis probes is shown in Figure 5.[92] The membrane region of a probe is usually made of semipermeable membranes materials with specific molecular weight cutoff. This tiny probe could be inserted into a specific region of a

tissue or experimental animal for analysis. During the operation, perfusion fluid with calibrator is pumped through the probe at a low and constant flow rate, usually between 0.1 and 5.0 μL/min. According to the concentration gradient, the molecules below the cutoff weight of the membrane may undergo exchange in both directions across the membrane. The dialysate containing analyte and calibrator will then collected for assay.[92] This method has been widely used for in vivo analysis of extracellular GSH in rat brain.[70, 93-95]

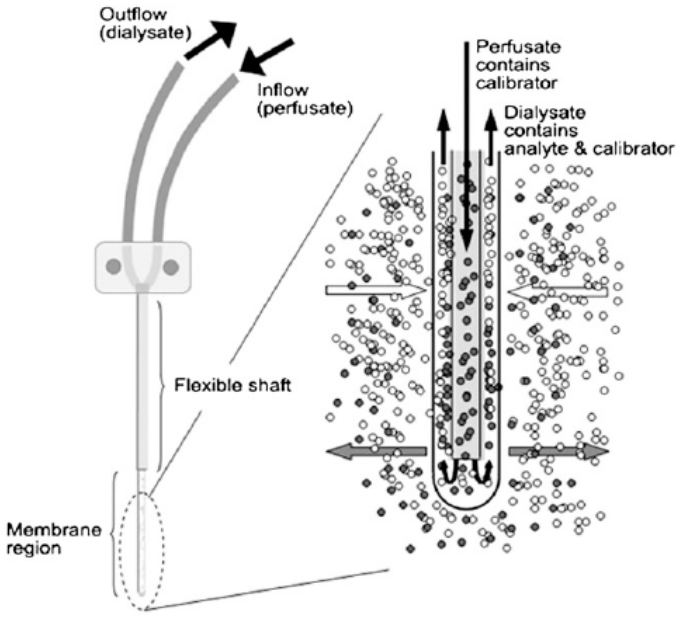

Figure 5. Microanalysis probe with concentric design[92]

Analyte of interest (open circle); Calibrator in perfusate (close circle)

Other procedures, such as protein removal and disulfide reduction, are often necessary for the subsequent analysis, depending on the analytes and the analytical technique used. As mentioned above, protein in the sample matrix may lead to the proteolysis of GSH. Besides, it also seriously reduces the separation efficiency and causes irreproducible problems in chromatographic and electrophoretic systems through adsorption on the inside wall of column. Other than acidification, adding organic solvent modifier and applying ultrafiltration are two

other ways to remove the protein. Organic solvents, like acetonitrile, acetone or methanol, show their advantage over acid reagents when a mass spectrometer is used as a detector. However, it is recommended to protect the thiol group first to eliminate the oxidation of GSH before adding organic modifier.[3, 96] Although it takes additional time to filter the sample, ultrafiltration introduces no other reagent or modifier into the system, which reduces the uncertainty and artifacts and is useful for better performance in the following separation or detection. Disulfide reduction is a requirement for total GSH analysis. Compared with enzymatic reaction and electrolysis, most of the researchers use reducing agent to achieving reduction in their experiments. Sulfhydryl-containing reducing agents (dithiothreitol, DTT, dithionite, DT, dithioerythritol and 2-mercaptoethanol), sodium or potassium borohydride, trialkylphosphines (tributylphosphine,TBP, tris-2(-carboxyethyl)-phosphine, TCEP, triphenylphosphine, TPP) and are the most common reagents in recent literature. Special attention should be paid to the specific characteristic of each reductant.[3]

1.2.2 Separation methods for GSH determination

Numerous analytical methods applied in GSH determination in different matrices have been summarized in some general reviews.[1, 3] Basically, these methods can be classified into two categories, separative and non-separative. Among all the separative methods, HPLC and CE are the most widely used ones. Other methods like TLC and GC and microfluidic chip are also presented in some papers. Common detectors used in separative methods are UV-Vis detector, diode array detector (DAD), electrochemical detector (ECD), MS detector and fluorescence detector (FLD). Although some studies showed that GSH could be detected by extended path-length UV-Vis detector without further derivatization, it is often advantageous to introduce tags

with strong chromophores or fluorophores to decrease the detection limit when using UV-Vis, DAD and FLD detection. Compared with carboxylic and amino group, the thiol group in GSH structure is always a much more popular target in derivatization due to its specificity. Meanwhile labeling with a fluorophore also provides GSH with an extra protection on its active thiol group. There are several rules for selecting a suitable reagent for derivatization. 1) The absorption wavelength, the excitation wavelength, or emission wavelength should meet the specification of the light source and detector; 2) The derivation should be carried out under comfortable conditions without disturbing or destroying the analytes of interest; 3) Interfering compounds should not be introduced into the system; 4) The reaction between analytes and derivatizing agent must be quantitative for accurate quantitation; 5) Fast reaction rate is required for pre-column, post-column and especially online analysis. 6) It is especially good for fluorogenic agent to have weak or no fluorescence before reaction, but have high quantum yield afterward. The most widely used reagents for chromophore introduction are Ellman's reagent (5, 5'-dithio-(bis-2-nitrobenzoic) acid, DTNB), Sanger's reagent (1-fluoro-2,4-dinitrobenzene, DNFB), monoiodoacetic acid (MIAA), N-ethylmaleimmide (NEM) and its analogues. Besides, there are other famous reagents used for fluorophore introduction, such as *o*-phthalaldehyde (OPA), monobromobimane (mBBr), 4-aminosulfonyl-7-fluoro-2,1,3-benzoxadiazole-4-sulfonate (SBD-F), Some structures of the above reagents are shown in Figure 6.

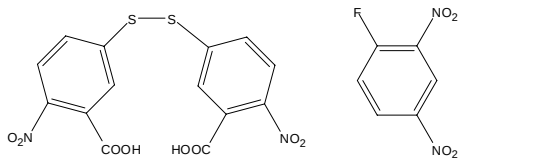

DTNB
(Elman's reagent)

1-fluoro-2,4-dinitrobenzene (DNFB)
(Sanger's reagent)

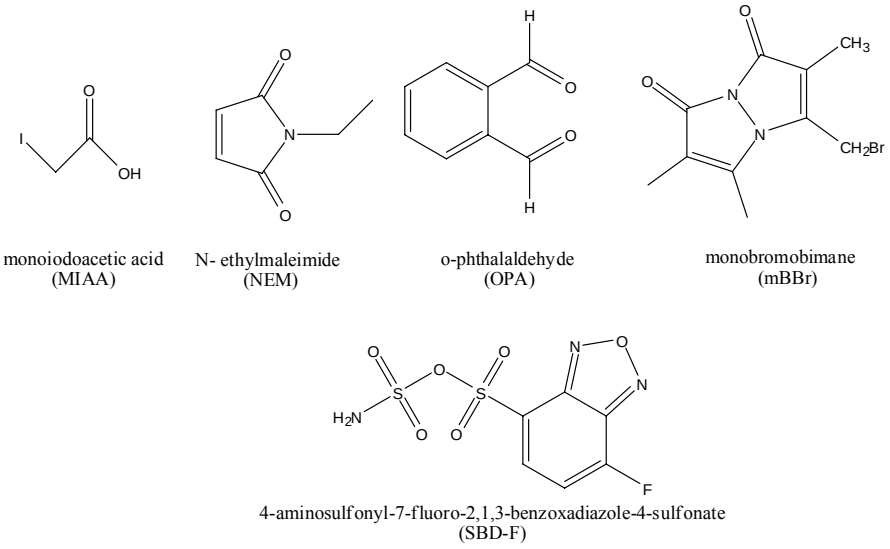

Figure 6. Structures of some common derivatizing agent

HPLC is well known for its advantages in fast separation, high efficiency and low sample consumption. Analytes are separated in HPLC column according to the difference in retention times caused by the equilibrium distribution of solutes between the stationary phase and mobile phase. Most GSH (and analogues) determinations performed by HPLC use octadecylsilica gel (ODS) as the stationary phase and are performed by reversed-phase (RP) mode. Detectors such as UV-Vis, DAD, ECD and MS are compatible with HPLC. Nozal et al. compared the concentrations of GSH and related compounds in rabbit eyes tissue by using HPLC with a 25x0.46 cm ODS column. UV detection was performed after a post-column derivatization with DTNB. The LOD obtained for GSH was 19 μg/L.[90] Yang et al. combined microdialysis and HPLC for in vivo monitoring of extracellular GSH concentration in rat brain. GSH and related compounds were first derivatized with fluorescent tag, methanolic mBBr, and then separated on a narrow-bore RP C_{18} column followed by fluorescence detection. Their results indicated that the basal extracellular GSH levels in brain cortex were 2.10±1.78 μM and there was a dramatic increase in the concentration of GSH after cerebral ischemia.[70] Shi et al. also presented the

combinational use of microdialysis and HPLC with electrochemical detection of the GSH in the brain of a freely moving rat. The LOD for their experiments was 2.5 μM.[95] A two-dimensional chromatographic system with parallel Hypercarb columns™ coupled with dual FLD was presented by Sakhi et al.. Plasma samples were first mixed with derivatization solution and injected into analytical column 1, where mBBr bounded GSH was trapped, and further onto analytical column 2. Separations were carried out in parallel on both columns. GSSG was separated and detected on second column with a post-column derivative agent OPA. The LOD for their systems was 0.140 μM.[87]

CE is another separative technique widely used in GSH determination. Under a high DC electric field, ionic species can be separated in capillary according to the difference in their charge and frictional forces. Different from HPLC, CE uses electroosmotic flow as a driving force rather than hydraulic pressure, which results in a flat flow profile instead of a rounded laminar flow profile. Besides, there is no mass transfer between phases in CE. As a result, band-broadening in CE is much less significant than that in HPLC, which contributes to its higher separation efficiency. Meanwhile, because the internal diameters of capillary used in CE are usually within the range of 25 μm-75 μm, CE requires lower volume of sample for analysis than HPLC does. In addition, high voltage applied in the CE system enables the separation to be performed at high speed and to be finished within several minutes. Because of all these advantages, CE has found its wide-spread use in GSH determination. Carru et al. used CE-LIF method to measure total plasma thiols. By adding N-methyl-D-glucamine into the buffer solution, baseline separation of cysteinylglycine, homocysteine, cysteine and glutathione was achieved within 9 min. The minimum detectable concentration of free thiols is 100 pM with a SNR of 3.[81] Lada et al. coupled CE with microdialysis by a flow-gated interface for continuously

monitoring thiols in vivo. Analytes were derivatized with mBBr before entering into the separation capillary and detected by a laser-induced fluorescence detector after separation. The on-line LOD for these analytes were in the range of 20-40 nM.[93, 97] Hogan et al. used CE to study GSH from a single human erythrocyte. Cells were first cultured with derivative reagent mBBr. During the experiment, one end of a capillary was inserted into a small drop of solutions containing cells. By applying a pulse of vacuum from the opposing capillary orifice, individual erythrocyte was drawn into an open capillary of 10 μm I.D.. Lysis of the cell was achieved by lysate solution or applying high electric field, upon which the content of the cells was separated by CE equipped with FLD. The detected value for a single cell was about $(7.5\pm0.55)\times10^{-4}$ M.[83]

1.2.3 Non-separation method for GSH determination

Presently, non-separative methods applied in GSH related measurements mainly include spectrophotometry, spectrofluorimetry and amperometry, etc..[3] One obvious merit these methods have compared with separative methods is that there is no need to separate the analytes interested from the matrices. Researches usually spend a lot of time in optimizing separation conditions, meanwhile, the equipment needed to perform separation are sometimes expensive. However, in order to obtain accurate and reliable results, non-separative methods require high selective ways to detect the analytes from a complex matrices background. One choice is to use some special labels which aim at analytes of interest specifically. Early in 1969, Tietze developed a sensitive spectrophotometric protocol to detect total glutathione. He found that the addition of GSSG or GSH to a model reaction mixture containing yeast glutathione reductase (GR) and reduced triphosphopyridine (TPNH) and DTNB would result in an excess color yield at 412 nm. And the rate of excess of color development depended on the concentration of glutathione in the reaction

mixture and was still detectable at concentration as low as 10 ng/mL. In addition, GSH and GSSG would be detected separately by pretreating the sample with NEM, which blocks the GSH in the system before analysis.[98] Liang et al. uses a 5-maleimidyl-2-(*m*-methylphenyl) benzoxazole (MMPB) as a fluorescence probe, which has a rather high selectivity for GSH to cysteine. Even with the presence of cysteine, a linear relationship was found in the range of 0-1.62×10^{-7} M with the LOD of 3.23×10^{-10} M for GSH by direct spectrofluorimetric measurement.[9] Another choice for selective detection is to use special electrochemical sensors for GSH detection. Inoue et al. modified a glassy carbon electrode by incorporating the coenzyme pyrroloquinoline quinine into a polypyrrole (PPy) film, which allowed a selective determination of GSH with a LOD of 11.2 μM.[10] In addition, nuclear magnetic resonance (NMR) is also a good method to determine GSH non-separatively. Trabesinger et al. used ^{1}H-magnetic resonance spectroscopy to determine the GSH in human brain in vivo. In their experiment, double quantum coherence filtering method provides good discrimination between the GSH signal and the interfering resonances of creatine, gamma-aminobutyric acid (GABA) and aspartate.[99, 100] Kennett et al. also applied NMR to study the exchange of GSH between intra- and extracellular GSH in human erythrocytes. By using H-1 spin-echo NMR to measure the intracellular glutathione redox status and applying C-13 (H-1-decoupled) NMR to determine the extracellular status, they realized the direct and non-invasive observation over time of the GSH status in both compartments.[101]

1.3 MICROFLUIDIC DEVICES WITH CONFOCAL LIF DETECTION

1.3.1 Theory of miniaturization

The concept of miniaturizaed total analysis systems (μTAS) or lab-on-a-chip (LOC) system was first brought forward by Manz et al. in 1990, in which they envisioned a system that incorporates all sample handling steps, such as sample pretreatment, chromatographic or electrophoretic separation, and detection, close together on one device.[102] This idea was the natural generalization of the rapid development in the promising field known as microelectro-mechanical systems (MEMS) in 1980s and contributed a lot to the practical needs for miniaturization, integration and portability in biotechnology, pharmacology, medical diagnostics and forensics, etc. Indeed, LOC system could be treated vividly as the shrinking of an entire laboratory to a chip. Because the realization of these lab functions on a chip relies on the controlling of fluid flow at micrometric length scales, a young discipline-MICROFLUIDICS-was created, which is aimed at the study of flows, simple or complex, mono- or multiphasic, circulating in artificial microsystems.[103] Although the main reason for miniaturization at the beginning was to enhance the analytical performance of the TAS as a new kind of chemical sensor, it was recognized that miniaturized device not only enables faster and more efficient transportations and separations, but also dramatically reduce the amount of required sample, carrier, reagent or mobile phase.[104] Attracted by all these advantages, more and more researchers have joined their effort in this young discipline since 1994. A lot of pioneering works in the development of the theory, technologies, analytical operations and applications are summarized in some excellent reviews.[105-108]

1.3.1.1 General

Flow injection analysis (FIA), chromatography and CE are three analytical techniques commonly used in experiments performed on microfluidic device.[102] FIA systems separate each sample from subsequent sample with a carrier reagent, which is convenient for automatic sample introduction in micro-channels.[109] Chromatography and CE, however, are two choices for achieving separation. Although there are some visible differences between separations carried out in normal capillary columns and on microfluidic chips, the theoretical basis for chromatography and electrophoresis on microfluidic device inherits a lot from the existing theories for these two separation methods in conventional analysis.[110]

The broadening of solute bands in an open tubular column in a chromatographic system occurs when the solutes travel through both inside and outside the separation column, the latter mainly concerned with the injection, detection steps and traveling through connecting tubes. The extent of spreading directly determines the efficiency of the separation. In an ideal experiment, sample with solute of interest will be introduced into the system as a narrow zone and travel across the column at a constant rate. However, in practice, the rates for individual solute molecules are not always the same, which constitutes the origin of band-broadening. There are three major contributions to the difference in velocity as the solutes travel through the column: first and foremost, the resistance to mass transfer between phases prevents instantaneous equilibrium; second, the inequalities of flow with radial position in the mobile phase, which is related with the parabolic flow profile of a laminar flow in a pressure-driven system. Diffusion of the solute in the radial direction compensates this effect to some extent; third, the molecular diffusion in the axial direction, which is also known as longitude diffusion. The plate height H (or the height of an equivalent theoretical plate, HETP) in Eq.1 includes most of the major

factors for band-broadening in open tubular column and it is always used as an important parameter for measuring column efficiency.[110]

$$H = H_S + H_M + H_L \tag{1}$$

where H_S, H_M and H_L are the terms of stationary phase mass transfer, mobile phase effect and longitudinal diffusion, respectively. Furthermore, by studying the origin and mechanism, we can derive a mathematical expression for each term as in Eq.2, Eq.3 and Eq.4.

$$H_S = \frac{k'}{(1+k')^2} \cdot \frac{{d_f}^2 \upsilon}{D_S} \tag{2}$$

$$H_M = \frac{1+6k'+11k'^2}{24(1+k')^2} \frac{r^2 \upsilon}{D_M} \tag{3}$$

$$H_L = \frac{\sigma_L^2}{L} = \frac{2D_M}{\upsilon} \tag{4}$$

where k' is the capacity factors, d_f is the characteristic distance in the liquid, such as the film thickness or droplet diameter and D_S is the diffusion coefficient in the liquid stationary phase. r is the inner radius of the column. D_M is the solute diffusion coefficient in the mobile phase and υ is the mean velocity of the mobile phase.

Compared with chromatography, the HETP for an ideal CE has no contribution from resistance to mass transfer between phases. Meanwhile, the flow profile driven by electro osmotic force (EOF) is flat rather than parabolic as in chromatographic separation.[111] Therefore, only the longitudinal diffusion term dominates the final separation efficiency and that is why CE usually has a theoretical plate number up to several hundred thousand, which is much higher than that for a chromatographic separation.[112, 113] Besides, technically, it is much easier and space-saving to apply EOF as a driven force than integrating series of mechanically moving parts, such

as micro valves and pumps for a chromatographic analysis on a compact microfluidic device.[105] From this point of view, CE is a better choice for separation on chip than chromatography.

1.3.1.2 Proportionalities

It is a useful approach to consider the proportionalities existing within a flow system when the dimension of the system goes down to micro scale. The parameters of interest are viewed as a function of the variables to be miniaturized, space and time. In this case, even with no knowledge of material constants, it is clear to predict the major trends of certain physical properties of the system. If we assume that a miniaturization is a simple three-dimensional downscaling process characterized by a typical length parameter l, we can compare relevant physical variable in similar systems with different sizes. The typical length l is the scaling factor of the miniaturization. There remains one degree of freedom for the mechanical parameters. Proportionality factors for some mechanical parameters in relation the characteristic length l are summarized in Table 1 for two important cases: time-constant system vs diffusion-controlled system.[102, 103, 112, 114]

In the case of some electrical parameters, the time scale must be constant in order for the definitions of the electric current, the electrical capacity and Ohm's law to be consistent.[102] There are three subsystems where one more parameter is given constant, namely, constant charge density (system a.I), constant electrical field strength (system a.II) and constant voltage (system a. III). Proportionality of some electrical parameters in relation to the characteristic length l under different systems is given in Table 2. Experiments are needed to show which system is the best description of the miniaturization.

In the case of time-constant system, the time scale is the same for the similar systems with different size. For example, if the pressure gradient required for simple transport or FIA

system is reduced proportionally according to the decrease in the dimension of the system, the analysis time will be constant. Therefore, we could use time-constant system to describe this situation. The advantage in downscaling simple transport or FIA systems lies in the conservation of carrier and reagent solutions. A 10-fold decrease in size would cause a 1000-fold decrease in

Table 1. Proportionalities of some mechanical parameters in relation to the characteristic length l

	(a) Time constant system	(b)Diffusion controlled system
Time, t	constant	l^2
Space, l	l	l
Linear velocity, u	l	l^{-1}
Volume flow rate, F	l^3	l
Pressure drop, Δp (laminar flow)	const.	l^{-2}
Voltage, V (EOF)	l^2	const.
Electric field, V/L, E (EOF)	l	l^{-1}
Reynolds number, Re	l^2	const.
Reduced flow rate, ν	l^2	const.
Reduced elution time, τ	l^{-2}	const.
Reduced pressure, Π	l^2	const.
Reduced voltage, Ψ (EOF)	const.	const.
Linear acceleration	l	l^{-3}
Angular velocity	const.	l^{-2}
Impulse	l^4	l^2
Force	l^4	const.
Energy (work)	l^5	l
Power	l^5	l^{-1}
Pressure	l^2	l^{-2}

Table 2. Proportionalities of some electrical parameters in relation to the characteristic length l

	(a) Time constant system		
Time, t	Constant		
Space, l	l		
Ohmic resistance, R	l^{-1}		
Electrical capacity, C	l		
	a.I	a.II	a.III
Electrical charge, Q	l^3	l^2	l
Voltage, V	l^2	l	constant
Electrical field strength, E	l	constant	l^{-1}
Electrical current, I	l^3	l^2	l
Magnetic field strength, H	l^2	l	constant

carrier or reagent comsumption. In a diffusion controlled system, the molecular diffusion, heat diffusion or flow characteristics control the separation efficiency. This is in agreement with standard electrophoretic band-broadening theory. According to Table 1 and Table 2, in a diffusion controlled system, the time scale is treated as a surface. A down-scale to 1/10 of the original size will reduce the related time variable to 1/100, but the voltage requirements remains constant. The main advantage for diffusion-controlling system is that a considerable higher rate of separation can be obtained upon miniaturization while maintaining comparable separation efficiency. Besides, as heat generated by the system is given by Eq.5, the reduced production of heat in a small size tube allow higher electrical field to be used, which will further increase the separation efficiency. This evidence again proves that EOF is a better choice than pump-driven flow for microfluidic devices.

$$Heat = \frac{V^2}{R} \cdot t \propto \frac{1}{l^{-1}} \cdot l^2 = l^3 \tag{5}$$

1.3.2 Confocal LIF detection

Presently, almost all the detection methods used in traditional chromatography have been applied to the detection on microfluidic devices. These methods range from chemiluminescence and electrochemicluminescence detection, fluorescence/nonfluorescence optical measurements to electrochemical detection, mass spectrometry and other less commonly used detection methods, such as Fourier transform spectrometer, flame analyzer, and atomic emission spectrometry, etc..[105-108, 115] Compared with other methods, LIF detection remains one of the most sensitive detection techniques applied in detection following chemical separation presently. Under the best conditions, the concentration LOD is on the order of 100 fM and the mass LOD is about a few tens of molecules. As the volumes of samples handled on the microfluidic devices are very small and usually at low concentrations, it has a more stringent requirement for a highly sensitive detector than other common separative methods. LIF is the best choice to accomplish detection when the analyte is at a low concentration, if the analyte is fluorescent itself or can be tagged with a fluophore.

Confocal is defined as "having the same focus". What this means in a confocal LIF system is that the focal point of the microscope objective lens forms an image where the pinhole is, these two points are known as "conjugated points". The pinhole is conjugate to the focal points of the objective lens, thus it is often known as a confocal pinhole. In conventional fluorescence detection, the sample is completely illuminated by the excitation light, thus all the sample is fluorescing at the same time. Although the highest intensity of the excitation light is at the focal point of the lens, the other parts of the sample do get some light and they do fluoresce, which causes the non-linearity in quantitative measurement and can be treated as one of the background noise sources. Mathematically, the final intensity or image at the detector is a

convolution of a three-dimensional incoherent light source and a certain defocused point spread function of an optical system.[116] In a confocal LIF system, detector only detects fluorescence generated from the focal point on a submicron thickness optical slice. All other light rays, such as fluorescence coming from out-of-focus planes, or fluorescence from the focal plane, but not at the focal point, laser light reflected or scattered from the cover glass and channel walls, will finally be blocked and filtered out by spectral and spatial filters before they reach the detector. Compared to regular fluorescence detectors, a confocal LIF detector has higher axial resolution and is able to control the depth of field. Besides, it also works well to eliminate or reduce the background noise and improve the SNR. All these advantages make confocal LIF a sensitive and accurate technique and ensure its status as a most sensitive technique for microfluidic device for minute amount of analyte. Figure 7 is scheme of a typical confocal LIF setup. A laser is used as the light source to produce a distinct and spatially constrained point source of illumination. The beam first passes through a laser line exciter filter and is reflected by the dichroic filter positioned 45 degree and focused onto the sample in the microchannel via a microscope objective. A pinhole is placed in front of the detector at the optical position that is exactly where the fluorescence from the focal point of the objective is focused after the tube lens. A band pass emission filter is placed after the pinhole to exclude light with unwanted wavelength. The dashed blue line in Figure 7 denotes the fluorescence generated by the sample above the focal plane, which is rejected by the pinhole before the detector. The straight line represents the fluorescence signal produced by the sample on the focal plane, which passes through the pinhole and finally reaches the detector. In a true confocal system, the excitation volume depends on the objective NA and on the entering laser beam diameter, while the collection volume depends on NA and the spatial filter diameter.[27]

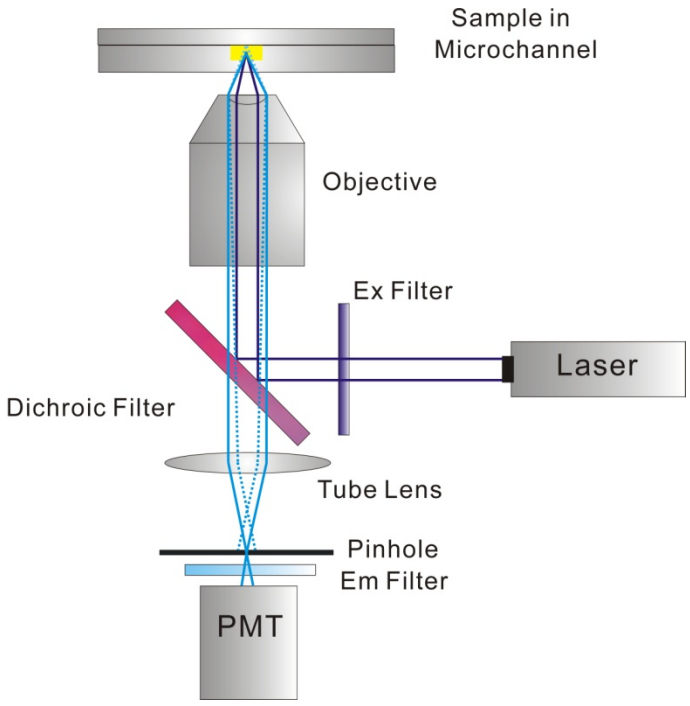

Figure 7. Scheme of a typical confocal LIF detector

Since the first introduction of LIF as a detection technique for CE in 1985 by Gassmann, Kuo and Zare,[117] LIF has attracted a lot of research interest because its high sensitivity extends to near the single molecule level. There are multitudes of papers that described LIF detection on CE and microfluidic chips. By incorporating CZE, sheath flow, LIF and an eyepiece fitted with a pinhole 200 μm in radius before PMT, Cheng and Dovichi achieved subattomole amino acid analysis in 1988, which represented an improvement of four orders of magnitude in the state of art for fluorescence detection of amino acid at that time.[118] In the following year, Wu and Dovichi published another important paper which gave a systematic discussion about each step in constructing a LIF detector of high SNR for CZE.[119] In one seminal paper by Mathies et al. in 1989, a theory for single-molecule fluorescence detection was described and used to analyze data from the photon bursts detection experiments of individual fluorophores passing through the focused laser beam.[120] A year later, they presented another paper in which they discussed the

strategies for high sensitive fluorescence detection by optimizing both the incident light intensity and the duration of illumination in the presence of both ground-state depletion and photodestruction.[121] Rather than collecting fluorescence at a right angle relative to the incident focused laser beam as experiments in the previous publications, Hernandez et al. first used same fluorite objective to focus laser beam and collect the emitted fluorescence in 1991. Their results on this confocal LIF detector represented an improvement of about three orders of magnitude with respect to previous LIF on-column detection.[122] All these pioneering papers laid a solid experimental and theoretical foundation for subsequent researches in the field of ultrasensitive confocal LIF detection and microanalysis. Recently, various laser sources and detectors have been introduced into the LIF system.[123-125] Parameters of optical components and its arrangements are further discussed according to their effects on experimental results.[27, 126, 127] More studies were aimed at applying confocal LIF for single cells and single molecule analysis on microfluidic devices.[127, 128]

1.3.3 Microfluidic chip and GSH determination

By far, most of the researches concerning GSH on microfluidic chips use a GSH as a model compound to test the separation of the system or to demonstrate the performance of single cell analysis. Pasas et al. performed the separation and detection of homocysteine and GSH from a solution by using a glass microchip with a gold/mercury amalgamated electrode. The separation was accomplished in less than 80 s at field strength of 360 V/cm.[129] Beside using pure commercial available GSH, intracellular GSH and ROS from some common cells human serum were also determined either by coupling offline extraction and microfluidic device analysis or by incorporating single cell lysis and analysis on one microfluidic chip. Qin et al. studied the effect

of arsenic trioxide and buthionine sulfoximine on GSH cell level by using microfluidic chip to study extracts from leukemia cells.[85] Long et al. integrated a nanoporous membrane as a filter into microfluidic chip for determination of GSH in lysate from human plasma and red blood cells without any off-chip deproteinizaiton.[130] Gao and Fang et al. developed a microfluidic system with functional integration of cell sampling, single cell loading, docking, lysing, and CE separation with LIF detection on a simple crossed-channel glass chip. Concentration of intracellular GSH in single human erythrocytes was determined to be $7.2x10^{-4}\pm3.3x10^{-4}$ M.[84] By applying a similar method, Ling and Fang et al. also realized simultaneous determination of ROS and GSH in the individual erythrocyte on an improved microfluidic chip. Different from the previous one, they introduced an additional tee intersection between the sample reservoir and the sample waster reservoir to avoid unwanted lysis and leakage of cells during the separation, which increased the stability of the channel and enabled multiple analysis on one chip.[86] Sun et al. built a novel multi-depth microfluidic chip with a weir structure in the separation channels to trap and lyse cells in the channel. The GSH and ROS in single human carcinoma cell were then separated and quantitated by using a LIF detector.[17] Instead of lysing the cell before analysis, Gao et al. used fluorescence images in a microchannel by using microscope coupled to a highly sensitive CCD to determine the GSH and ROS inside single intact cells flowing through a simple U-shaped single channel.[131] Miyaki et al. modified the surface of a polydimethysiloxane (PDMS) microchannel with poly (L-glutamic acid) to maintain its long-term stability under consecutive electric field. This microfluidic device was further used to determine the homocysteine and GSH in pretreated human serum.[132]

To the best of my knowledge, there is no report about online analyzing extracellular GSH from slice culture on microfluidic chip up to now.

2.0 DEVELOPMENT OF A CONFOCAL LIF DETECTION SYSTEM

To build a sound confocal LIF detection system, one needs to take into account the following key aspects. 1) Selecting an optimized set of optical components. Parameters for a certain optical component, such as the type and wavelength of the laser, cut-on and cut-off wavelength of a filter set, magnification and numeric aperture (NA) of the microscope objective, etc., need to be carefully selected according to the ultimate goal of a specific analysis. 2) Designing an opto-mechanical assembly. This usually includes building a platform for microfluidic device, choosing series of holders and stages to support and arrange optical components into a whole system. A good arrangement of optical components will not only ease the beam alignment, but also increase the sensitivity and decrease the LOD of the detection system. 3) Developing a controlling program. Computer control allows the automation of the detection system. It should integrate different functions and offer an easy access for user to have a convenient control of the whole system. Thus it is wise to incorporate major functions, such as data collection and pretreatment, voltage and current monitoring, high voltage power supply (HVPS) manipulation, sampling control, into one program.

2.1 OPTIMIZATION OF OPTICAL COMPONENTS

2.1.1 Laser

According to confocal theory, only the fluorescence signal generated from the focal point will be detected by the detector. It is necessary to use a laser as an excitation source and focus it into a small spot to get a strong signal. Laser beams are well known for their good qualities, such as monochromaticity, coherence, and high collimation. Within a certain range, the signal and background are expected to increase linearly with the laser power. However, under the shot limit condition, the noise in the background is only proportional to the square root of the laser power. Thus higher irradiance of a focused laser beam also produces better LOD than that of an incoherent light source.

One of the most important criteria in choosing a suitable laser source is its wavelength. It must match the absorbance spectrum of the analyte. As we are going to use Thioglo-1 to label GSH in the following analysis (the reason of choosing this dye will be further discussed in the later section), the excitation and emission spectra of GSH tagged with Thioglo-1 must be examined first. Figure 8. shows the excitation and emission spectra of labeled GSH taken with a SpectraMax M2 (Molecular Devices, Sunnyvale, CA). The concentrations for GSH and Thioglo 1 are 52 μM and 20 μM respectively. The spectra were taken right after mixing of the GSH and Thioglo 1 stock solutions at 24.8 ºC. Figure 8 indicates that the excitation and emission maximum are 370 nm and 502 nm for Thioglo 1 conjugated with GSH, which are different than the literature values, excitation 379 nm and emission 513 nm, provided by the product catalog. Possible reasons may be the difference in concentration or variance in the forms of thiol group. The final wavelength of the laser is chosen to be a little higher than 400 nm based on several

reasons. First, although 370 nm is the peak excitation wavelength for the GSH-Thioglo 1 conjugate, it is falls out of the wavelength range of visible light, 380–750 nm, for the human eye. Thus it will cause predictable difficulty during the beam alignment. Second, the closer the wavelength is to the ultraviolet portion, the more chance that other analytes in the sample and different materials in optical path may be excited and fluoresce, which will increase the background. Third, it is less expensive to get a laser with longer wavelength.

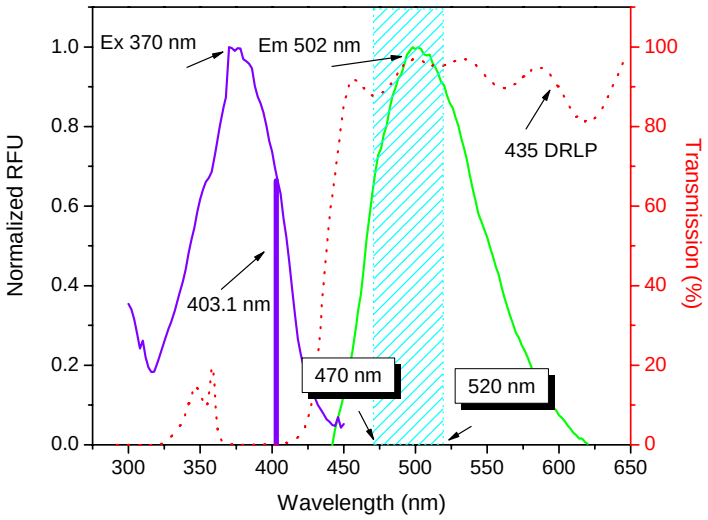

Figure 8. Excitation and emission spectra of GSH -Thioglo 1

Another factor which dominates the selection of a laser is its spatial mode quality. Generally, continuous-wave (cw) lasers, such as the argon ion laser, possess high spatial coherence and may be focused to a few micrometers spot size. Pulsed lasers usually have poor spatial quality and are hard to focus to a small spot. On the other hand, pulsed lasers tend to have much higher intensity in a very short time compared with cw lasers; this will lead to saturation and photo-degradation of dye, which is harmful for the analysis. Finally, the stability of laser itself is pivotal to obtain shot-noise limited performance and high LOD.[119]

Although thousands of types of lasers have been discovered literally, few of them have found practical application. The widely used lasers can be classified into four categories: gas discharge lasers, semiconductor diode lasers, optically pumped lasers and "others", a special portion which includes chemical lasers, gas-dynamics lasers, x-ray lasers, and so on. Gas discharge lasers, like Helium Neon Lasers (HeNe lasers), Helium Cadmium lasers (HeCd lasers), Noble-Gas ion lasers, etc., provide exceptional reliability and superior optical characteristic. However, this type of lasers is usually very bulky due to its nature, which is not fit for microfluidic systems. Besides, the selectable wavelengths are determined largely by the active gas atoms used, thus provide not much freedom in wavelength selecting. The benefits of using a semiconductor diode laser include high optical efficiency for greater output power, compact size and low cost. However, this type of lasers must take advantage of external optics to yield a high quality output beam. Diode pumped solid state (DPSS) laser is a class of optically pumped lasers. It uses a semiconductor diode laser to pump a doped laser crystal. A nonlinear doubling crystal is also placed inside the laser cavity in close proximity to the lasing medium for generating a visible output. Rather than giving off the fundamental laser frequency of the crystal, the second harmonic generated by the doubling crystal is transmitted as the final laser beam. DPSS lasers combine the excellent beam quality of a gas laser with the small size and efficiency of a diode laser, and produce output at discrete wavelengths throughout the visible spectrum with low cost. Based on the above reasoning, we chose a DPSS cw laser produced by CrystaLaser (Reno, NV) as the illumination source. It is equipped with an adjustable power supply controller. Table 3 lists some of the main parameters for this laser. The output power for our system is adjustable from 0mW to 20 mW, which provides us the opportunity to find the optimum power for our specific dye. A Gaussian 20 mW beam focused to a 1-μm radius spot size will produce a peak irradiance

of over 10^6 W/cm^2 and in real operation the irradiance should be held to a value less than 10^5 W/cm^2 to eliminate saturation and possible photodegradation in fluorescence detection.[119] Thus output power range of 0 to 20 mW suffices for our system.

Table 3. Main parameters for BCL-020-405-CL2005 system

Parameters	Values
S/N	2710055-3211
Wavelength	403.1 nm
Output Power	20 mW Up to: 0-20 mW adjustable
Transverse Mode	TEM_{00} mode, M^2=1.2
Longitudinal Mode	Several longitudinal modes
Beam Diameter ($1/e^2$)	1 mm
Beam Divergence	0.6 mrad (full angle)
Output Stability	1% over 24 hours
Noise (rms)	< 0.5%
Operation Voltage	90 to 250 VAC
Dimension(mm)	30x30x120

2.1.2 Microscope objective

The microscope objective is one of the core components in a confocal LIF system. It focuses the laser beam into a tiny spot onto the sample in the microfluidic channel and collects the fluorescence signal generated by the sample and transmits it into the following optical path. There are several key parameters which determine the performance of an objective.

Numerical aperture (N.A.) is defined as the refractive index (n) of the immersion medium times the sine of the angle made by the marginal ray with the optical axis. It is closely related with the light collection efficiency as in Eq. 6.

$$\text{Collection Efficiency} = \sin^2\left[\frac{\arcsin(N.A./n)}{2}\right] \tag{6}$$

Therefore a lens of high N.A. is required to obtain high collection efficiency. For example, without special immersion medium, a lens with a N.A. of 0.6 will collect 10% of the emitted light, while a lens with a N.A. of 0.1 will only collect 0.3%. Objectives with higher magnification usually have greater N.A.

Optical aberrations occur in various forms for objectives, which include spherical aberration, chromatic aberration and other geometrical aberrations, such as astigmatism, field curvature and chromatic aberrations. Expensive objectives usually have better level of correction for these effects mentioned above than an inexpensive one. The highest level of corrections (and expense) is found in apochromatic objectives. These objectives are corrected chromatically for four colors, deep blue, blue, green and red. And they are spherically corrected for two or three colors, deep blue, blue and green. Fluorites or semi-apochromats have the middle level of correction. They are corrected chromatically for red and blue light, usually closer to the green focus and spherically for two colors, blue and green. Achromatic objectives are the least expensive one, which are corrected chromatically to bring red and blue light to a common focus. Besides, they are corrected for spherical aberration for the green color. In addition, some objectives are also corrected for curved image, which is well known for plan correction. Different from color micrography, a confocal LIF system employs only single wavelength as an excitation light and collects only a narrow band width of fluorescence signal, it is not necessary to use objectives with highest correction level.

Most transmitted light objectives are designed to image specimens that are covered by a cover glass. And the thickness of this small cover slip is standardized at 0.17 mm for most applications. General purpose objectives are designed for this thickness. However, some special objectives have a correction collar adjustment of the internal lens elements to compensate for the variation in thickness of the cover glass. Because the thickness of the base glass has a thickness of 1.0-1.1 mm, it is important to choose an objective with higher allowance for the thickness of the cover glass.

The working distance (W.D.) is the distance between the objective pupil lens and the top of the cover glass when the specimen is in focus. In most cases, the W.D. is inversely related to the magnification of the objective. It is safer to have an objective with ca. 3mm or longer W.D due to the mechanical platform for the microfluidic devices.

A LUCPLFLN 40x objective from Olympus (Center Valley, PA) has been selected to use in our confocal LIF system. It belongs to the UIS2 (infinity-corrected) series and is a plan-fluorites objective with a cover glass correction collar from 0-2 mm. The W.D. for this objective is between 2.7-4 mm, which is also within the safe distance for our system. The light collection efficiency is also acceptable under a N.A. of 0.6. Table 4. includes some of the main parameters for this objective. A LUCPLFLN 20x objective with focal length of 9.0 mm and W.D. of 6.6-7.8 mm is also used in some of the experiments mentioned below to test the performance of the system.

Table 4. Main parameters for LUCPLFLN 40x

Parameters	Value
Focal Length (mm)	4.5
N.A.	0.6
W.D. (mm)	2.7-4
F.N.	22
Cover Glass Thickness (mm)	0-2
Immersion	No
Correction Ring	Yes
Ultra Wide Anti-reflection Coating	Yes
Bright field	Excellent
Dark field	Good
DIC	Excellent
Polarized Light	Good
Fluorescence (B, G Excitation)	Excellent
UV Fluorescence (at 365nm)	Excellent

2.1.3 Photon detector

Fluorescence signal generated by the sample will finally be converted into electronic signal for post processing, analysis and storage. Photon detectors are sensors of light or other electromagnetic energy and are capable of translating optical signals into electronic signals. Generally, the detector produces a photocurrent upton the strike of photons and a voltmeter digitizer placed across the load resister produces a signal. In most cases, the light level is not high enough and needs an additional transimpedance amplifier (TIA) to amplify the photocurrent and then converts into a voltage output. Conventionally, there are three types of photon detectors widely used in low light detection in the 200-1150 nm range, namely photodiode (PD), avalanched photodiode (APD),[133-135] photomultiplier tube (PMT).[122, 124, 136, 137] To choose a suitable detector for a certain application, some important factors must be considered, which include gain, quantum efficiency (QE), SNR, active area of the detector, wavelength interested, response time and cost.[138]

The main component in a PD is the pn junction diode. The absorption of electromagnetic radiation causes promotion of electrons from the valance band to the conduction band and the formation of electron-hole pairs in the depletion region. When the rate of light induced charge carrier production greatly exceeds that due to thermal processes, the limiting current under reverse bias is directly proportional to the incident radiant power. These devices often show excellent linearity over six to seven decades of incident radiant power; however, the responsitivities are typically much lower than those of PMTs, because of lacking the internal gain as that in PMTs. The reverse bias across the pn junction is set to be lower than the breakdown voltage; sometimes there is even no external bias.

APDs are typically operated in the reverse breakdown region (larger than 100 V) of the pn junction and provide internal gain from 1 to 1000, Thus they often treated as PD with gain. Typically, it has a high sensitivity unmatched by PD and quantum efficiencies at > 400nm unmatched by PMTs.

PMTs are vacuum tubes. Photons enter the tube, strike the photocathode, get converted to an electron and the resulting current is multiplied by the dynodes. The operating voltage for PMTs is usually between 500 V to about 1200 V with gains of 10.[6]

Quantum efficiency (QE) is an important index for a photon detector. It is defined as the ratio of the number of photoelectrons ejected to the number of incident photons and can be calculated from photosensitivity S (A/W) by Eq. 7. One of the limitations when using PMTs is that the QE of PMTs is much smaller than that of PDs or APDs. For example, a gallium-arsenide-phosphide cathodes found in the most sensitive PMTs have QEs of better than 40% compared to the 85% peak QEs offered by PDs or APDs.

$$QE = \frac{S \times 1240}{\lambda} \times 100\% \tag{7}$$

With a high light power, APDs have the best SNR. The SNR for PDs are generally only as good as that of PMTs under best conditions and both of them can not match that of APD. However, with a low optical input, even at low speed (bandwidth) of light, PMTs offer a better SNR than both PDs and APDs with amplifiers. Under this condition, PMTs is operating in the shot-noise limit, while the PD and APD are limited by the amplifiers.[139]

When active area is concerned, APDs are typically limited to 10 mm^2 or less, while PMTs can have areas as large as 50 cm^2. Most PMTs provide little sensitivity in the NIR spectral region (beyond 850 nm), but PD or APD are sensitive up to 1100 nm. Besides, the rise times for these three detectors are all very short (1-10 ns) and they are all applied in experiments requiring

fast response. However, PMTs are generally used where really low light levels need to be detected, while APDs are used where the light level is too low for a standard PD but too bright for a PMT or where a magnetic field is present. In general, PMTs work better in the green and APDs are used more in the application in the red or near infrared range.

In our case, the emission light has a peak wavelength around 500 nm; meanwhile the signal from the confocal LIF system is relative weaker than that in normal fluorescence detection. We finally decided to use a head-on metal package PMT module H5784-01 from Hamamatsu Photonics (Bridgewater, NJ). Some of the main parameters for our PMT are listed in Table 5.

Table 5. Main parameters for H5784-01

Parameters			Value
Cathode Type			Multialkali
Peak Sensitivity Wavelength (nm)			400
Spectral Response (nm)			300-850
Frequency Bandwidth (kHz)			DC-20
Max. Output signal Voltage			10V
Cathode	Luminous Sensitivity (μA/lm)	Min	80
		Typ.	150
	Radiant Sensitivity (mA/W)*1		60
Anode	Voltage Output Depending on PMT Dark Current (mV) *2,*3	Typ.	0.4
		Max.	4
Offset Voltage(mV) *2		Typ.	±3
Ripple Noise (peak to peak)(mV) *2,*4		Max.	2
Settling Time(s) *5			2
Rise Time (ns)			0.78
Effective Area Φ (mm)			8
Dimension(mm)			22x22x60

*1: Measured at the peak sensitivity wavelength;

*2: Control voltage is +0.8 V;

*3: After 30 minute storage in darkness;

*4: Cable RG-174/U, Cable length 450 mm, Load resistance = 1 MΩ, Load capacitance= 22 pF;

*5: The time required for the output to reach a stable level following a change in the control voltage from +1.0 V to +0.5 V.

There are several major advantages of using module. First, our desired wavelength of 500 nm is near the peak sensitivity wavelength of this PMT. Second, the dark current and the ripple noise of this module are very low. Third, it is quite compact and includes a low-power consumption high-voltage power supply and a low noise amplifier together with a metal package photomultiplier tube. Fourth, the head-on type has a circular input window with a diameter of 8mm, which is much easier than a side-on module during beam alignment. Last but not least, the rise time for this module is fast, which is fit for detection following separation carried out in the microchannels.

2.1.4 Filter set, lens and mirrors

There are two kinds of filters in our detection system, spatial filter and spectral filters. A pinhole can be used as the spatial filter of the system. The diameter of the aperture depends on the area of the sample we want to analyze. The smaller the range of the sample we want to analyze, the narrower the aperture it should be and therefore the less noise from the background would pass through the pinhole. We prepared several pinholes with various fixed aperture diameters, ranging from 50 μm to 600 μm. The final diameter will be determined during the experiments. The selection of spectral filter set largely depends on the light source used and the excitation and emission spectra of the analyte (see Figure 8). A set of spectral filters usually includes an excitation filter, a dichroic filter and an emission filter. An excitation filter is placed after the light source, which is used to block light with unwanted wavelength from entering the system. A dichroic filter is applied in the system for two reasons. First of all, it reflects most of the laser beam and directs it towards the sample; secondly, it allows the passage of fluorescence collected by the objective while reflecting efficiently most of other light below its cut-on wavelength along

another channel in the optical system. An emission filter can be a long pass filter or a band pass filter depending on the actual experiment. Compared with long pass filter, a band pass filter is more aimed at the spectral region around the main peak of the emission spectrum. This serves to capture the most specific energy from the analyte rather than to capture the entire spectral region, and also, by keeping the overall filter bandwidth narrower than the 100nm range of the analyte, to reduce potential background artifacts.

In our optical system, we applied a XF2040 (435DRLP) filter as a dichroic filter and a 3rd 470-520 nm band pass filter as the emission filter, both of which are obtained from Omega Optical, Inc (Brattleboro, VT). The diameter of the dichroic filter is 22 mm. The transmission spectrum of this 435DPLP is shown in Figure 8. The 50% peak transmission is at 435nm, and the transmission at 403nm and 500 nm are around 0.19% and 96.8% respectively. This is quite compatible to wavelength of DPSS laser and the emission spectrum of the analyte. The key parameters for the emission filter are lists in the Table 6. The 3rd millennium bandpass filter applies Alpha technology and has very sharp edge steepness and it applies special coating assembly aimed at eliminating auto-fluorescence, improving transmitted wave front and lengthening filter life. Besides, transmission range of its spectrum is just around the emission peak of our analyte with the peak transmission of 83%. We didn't add the excitation filter right now for several reasons. The monochromaticity of our laser source is very good. In addition, the blocking provided by the dichroic and emission filter should be good enough to attenuate the laser line.

Table 6. Main parameters for emission filter

Parameters	Cut-On (nm)	Cut-Off (nm)	Average Transmission (%)	Edge Tolerance (nm)	Attenuation Range (nm)	Attenuation (OD)	Diameter (mm)
Value	470	520	83	±3	UV-1.3xCut-Off	>>>5	25

Because the fluorescence collected by the infinity corrected objective will travels in the form of infinity parallel rays after it passes through the objective, it is necessary to have a lens after the objective to focus the fluorescence signal to the pinhole. The focal length of this lens is depend on approximate location of the pinhole in the system. We chose an achromat doublet (G063215000, Linos Photonics, Inc, Milford, MA) with a focal length of 120mm and clear aperture of 25.4mm for our setup. It consists of a convex crown glass lens with low dispersion (color splitting) and a concave flint glass lens with a high dispersion. The advantage of using a doublet lens over singlet lens is that doublets correct for spherical as well as chromatic aberration. Meanwhile, they are often superior to simple lenses for focusing collimated light or collimating point sources, even in purely monochromatic light.[140]

Another important optic component in the system is the front surface mirror used to redirect the light path 45 degree to another channel. A silver elliptical plane mirror with a size of 22.4x31.5 mm is selected for our system. (G340523000, Linos Photonics, Inc., Milford, MA) It has the highest reflection (>95%) for 450 nm to 12 μm wavelength and a surface flatness of 1/10 λ, which is well suited for our system.

2.2 DESIGN OF AN OPTO-MECHANICAL ASSEMBLY

In order to reduce noise from vibration, the whole opto-mechanical assembly is built upon a 19″x23″ composite breadboard (NT54-252, Edmund Optics Inc., Barrington, NJ). We adopted a parallel mode in assembling laser and collection optics, where the laser beam and fluorescence signal entering the detector are parallel with each other as indicated in Figure 9. By sitting the laser (5), the optical tower and the stage C for pinhole (6), emission filter (7) and PMT (8) on top of a single rail with readings, the beam alignment becomes very easy. Meanwhile, this linear arrangement saves a lot of space for stage A.

Stage A is where the microfluidic device and cell dish with samples get supported and controlled. It is composed of an aluminum platform and an x,y,z-linear stage mounted on a heavy duty rod. This three dimensional stage allows the positioning to 1μm increments in each dimension. The design of the aluminum platform on stage A is shown in Figure 10. Each component on this platform is drawn to scale. An aperture with a size of 40 mmx15 mm is located close to the center of this platform, which has a trapezoid cross section and provides an easy access of the objective to the bottom of the microfluidic devices. Four slide bars will be fixed around the aperture by screws to hold the device in position. On the up left corner of this platform is the connector for the x,y,z-linear stage. Five circles with a diameter of 35 mm are holders for cell dishes. There are other several M4 holes distributed around the margin of the platform and they are mainly used to fix electrode arms supporting wire and electrode from the HVPS.

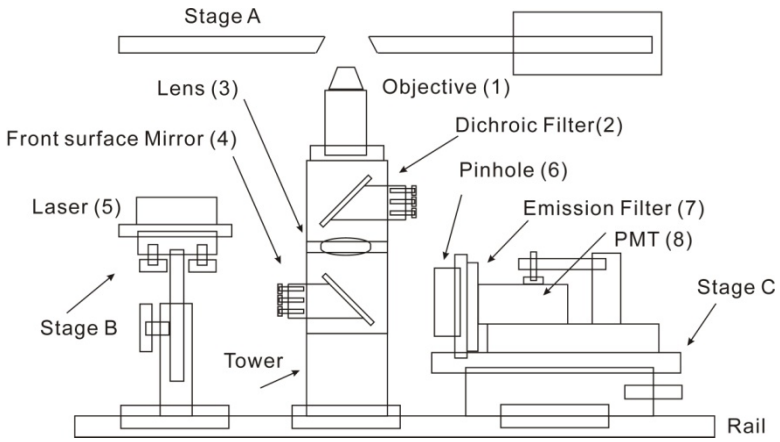

Figure 9. Sketch of the confocal LIF system

The main part in stage B is a small tilt table. The laser head is mounted on top of it horizontally with output surface of the beam towards the dichroic filter. The angle of beam can be finely adjusted by turning three spring thumbscrew adjusters at the bottom. The height of the beam can be regulated by the height of the post below the table.

Stage C is sitting on an x-linear stage attached to the opposite side of the rail. It combines three optical components together, the pinhole, the emission filter and the PMT. Figure 11 is a planform of this stage. A square bracket with a 33 mm x 33 mm through hole in the middle is attached to on one end of the stage C. This bracket is used to mount the pinhole positioner on one side and the emission filter holder on the other side. The size of this bracket is specially calculated to make sure the pinhole and emission filter is closely attached to each other in order to avoid miscellaneous light coming from the environment. PMT is held in position by another separate table, which is also fixed on the stage C. The head of the PMT is right against the holder of emission filter and forms a line with pinhole and emission filter together.

The other important part of the system is the optical tower standing in the middle of the rail. It is mainly composed of three 40mm cubes frame piled up to each other. On the top of the

tower is the objective (1) mounted on top of the first cube with an adaptor. The dichroic filter (2) is fixed on a beam steering mirror holder and takes up the top first cube. It changes the laser beam transmitting through one face of the cube 90 degree to the objective. The front surface mirror (4) is also fixed on a similar holder and resides in the second cube. It reflects the focused signal by the lens (3) mounted in a plate between the first and second cubes and redirects it towards the pinhole. This two steering mirror holders have three thumbscrew adjusters to finely adjust the angle and position of the filter and mirror, which are convenient for beam alignment.

An actual photography of the system is given in Figure 12, which is in a similar arrangement as the sketch in Figure 9.

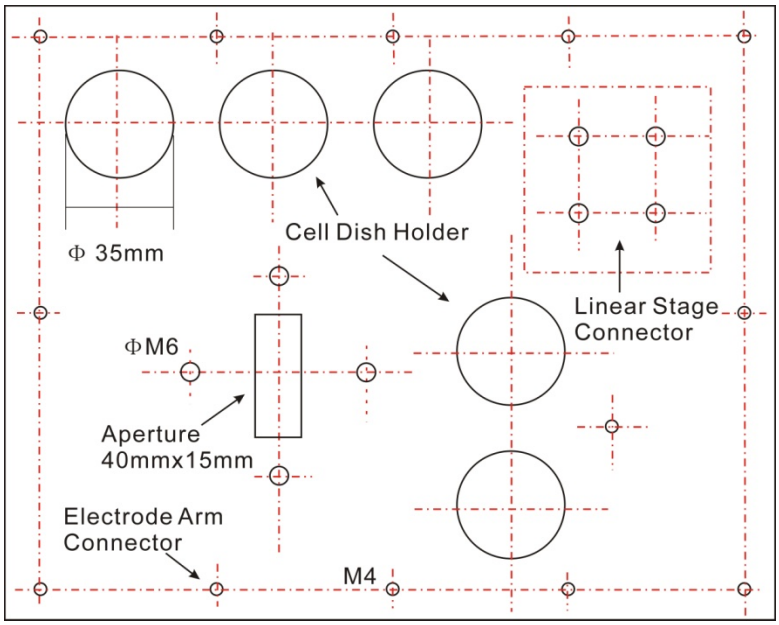

Figure 10. Top view of the metal platform on stage A

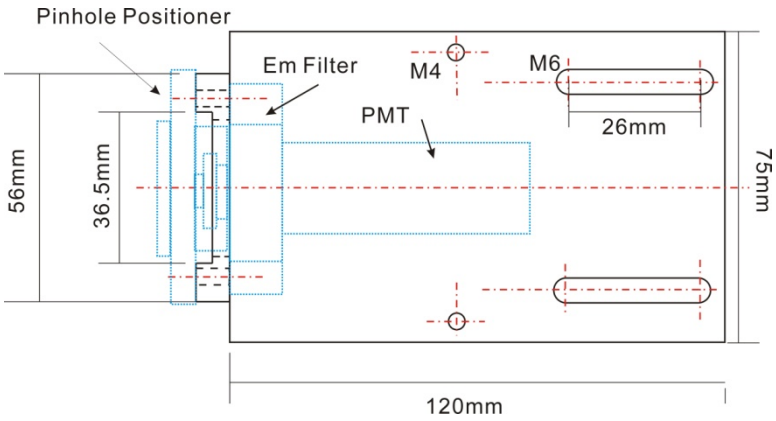

Figure 11. Top view of the stage C

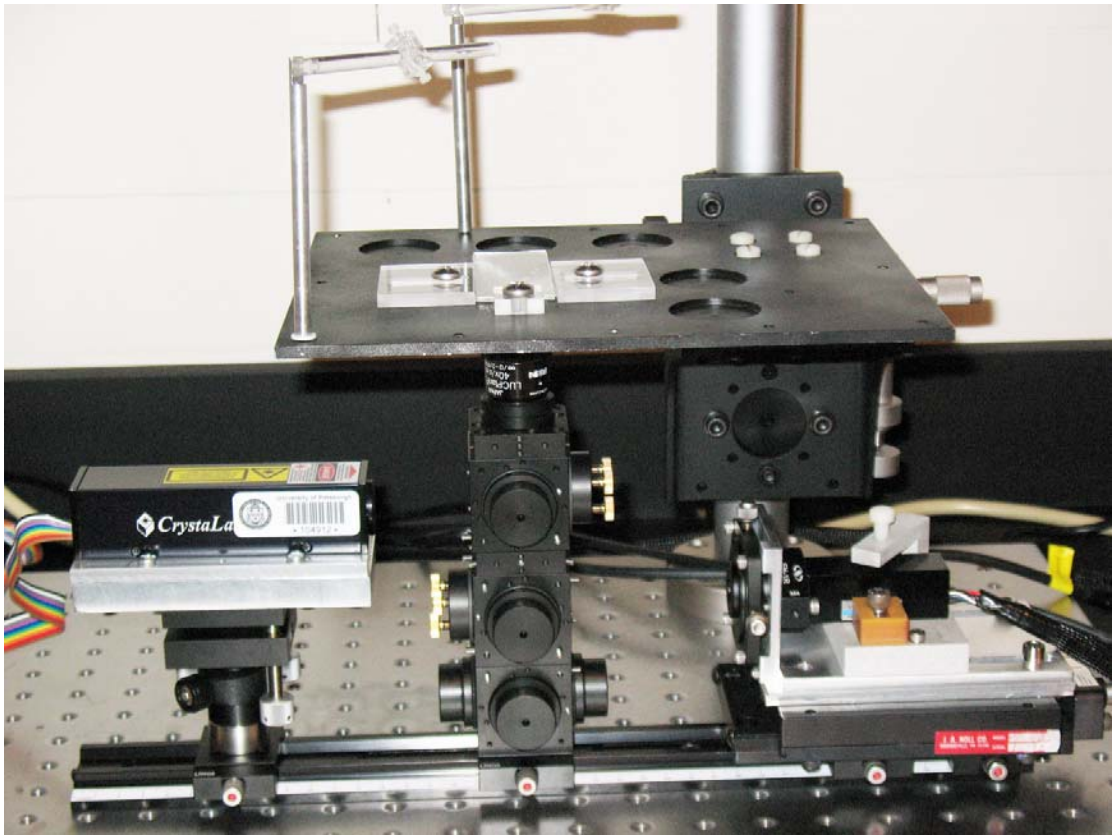

Figure 12. Photography of the confocal LIF system

2.3 DEVELOPMENT OF A CONTROL PROGRAM

The program used to control the detection system is developed with LabVIEW 8.2 (National Instruments, Austin, TX). LabVIEW is a visual programming language commonly used for data acquisition, instrument control, and industrial automation on a variety of platforms. The programming language used in LabVIEW, called G, is a dataflow programming language. Execution is determined by the structure of a graphical block diagram on which the programmer connects different function-nodes by drawing wires. These wires propagate variables and any node can execute as soon as all its input data become available. According to the functions we want to realize, this control program can be divided into four modules, namely, data acquisition and HVPS monitor, PMT voltage control, HVPS control, and sampling control. The basic principles that guide the programming are “simplicity” and “user friendly”. A 68 pin NI-PCI-6221 data acquisition (DAQ) card (16 bits resolution for analog input or output), a CP-68LP connector block and a SHC68-68-EPM cable are also obtained from National Instruments to cooperate with the program.

Data acquisition is the key function in the control program. There are three analog input channels employed in this process. One of them is used to collect signal from PMT. The other two are used to monitor current and voltage change of HVPS. Current signals from the PMT are first converted into voltage by its internal amplifier and then are transferred to the DAQ device. A digitizer on the device uses an accurate internal sample clock to determine the sampling rate (up to 250 KS/s), which can be set by the user through the user interface (also called front panel), and converts the input signal to digital values. These digital data are temporarily stored in a buffer region allocated by the program and then pass through a sub virtual instrument for averaging and are finally plotted on a chart on the front panel and written into the specific file.

The main parameters which can be controlled by the user through the front panel are listed in Table 7. Besides, there are three charts on the front panel, which function as instant monitors of the whole experiment.

The PMT module used in our system has a built-in low-power consumption (±15 V) high voltage power supply and a low noise amplifier. Besides, it has an additional pinout for external voltage control, because the voltage applied on the anode and cathode of the PMT is directly related with its sensitivity and noise level. We assign an analog output channel on the DAQ device to complete this function. A low voltage ranging from 0.25 to 0.9 V can be controlled by the user through the front panel of the program, which is consistent with what is defined in the datasheet of the PMT. During the experiment, users have the option to lock or unlock the voltage at a certain value.

Table 7. Main parameters for data collection

Parameters		**Value**
Channel	Max. (V)	Up to 10
	Min. (V)	Down to -10
Sampling Rate (KS/s)		0-250
Averaging Functions	Type	Linear/ Exponential
	Time (ms)	10/20/50/100
	Windows for DC and RMS	Rectangular
		Hanning
		Low Side Lobe
	Output Function	DC only
		RMS only
		DC and RMS
File/Process Control		Save/Run/Stop

The state and voltage control of the HVPS is accomplished by using three digital input & output channels (DIOs) and another analog output channel on the DAQ device. There are three states for the HVPS, namely “output”, “float” and “ground”, which is accomplished by the cooperation of three DIOs. Figure 13 indicates the relationship between three DIOs and relay 1, 2 and an enable/disable switch inside the HVPS. The connection between the levels of the DIOs and the state of the electrode is also listed in Table 8. A table-like structure is used as the interface for voltage input by the user. Each line in the table includes three parameters, line index, voltage value and timing. The program executes the commands in the table set by the user line by line and reinitialized the voltage to the default, 0 V, after the completion.

As we have designed to use a gated sampling mode on the microfluidic device for continuous monitoring GSH concentration in the extracellular space, an additional relay 3 is needed to control the sampling channel switching between ground (analysis) and float (sampling). Two modes, manual sampling and auto sampling, are designed in the control program. When the sampling mode is set to be manual, users can decide the sampling time and change the sampling channel from ground to float by clicking the START button. The channel will return to ground after the time is past. If the auto sampling is selected, users are allowed to use the front panel to set more parameters, such as initial delay, interval between each sampling and repeat times. The program also has a synchronization option, by selecting which the sampling will start at the same time with the data acquisition.

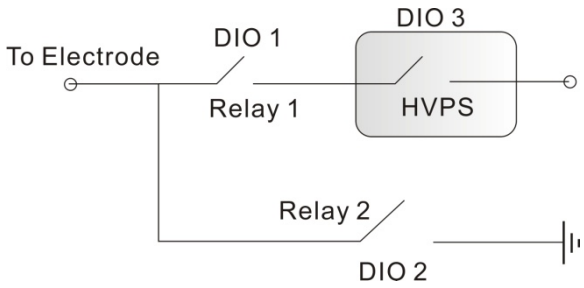

Figure 13. Sketch for the three DIOs controlling three states of the HVPS

Table 8. Connection between levels of DIOs and the state of the state of the electrode

Level of DIOS			State of the Electrode
DIO1	DIO2	DIO3	
1	0	1	HV
0	0	0	Float
0	1	0	Ground

Finally, the program has a safe “SHUT DOWN” button. If anything unusual happens in the middle of an experiment, user can disable the power supply, PMT and sampling, stop the acquisition and reinitialize every thing into its default value by simply clicking that button. A screenshot of the control program is given in Figure 14.

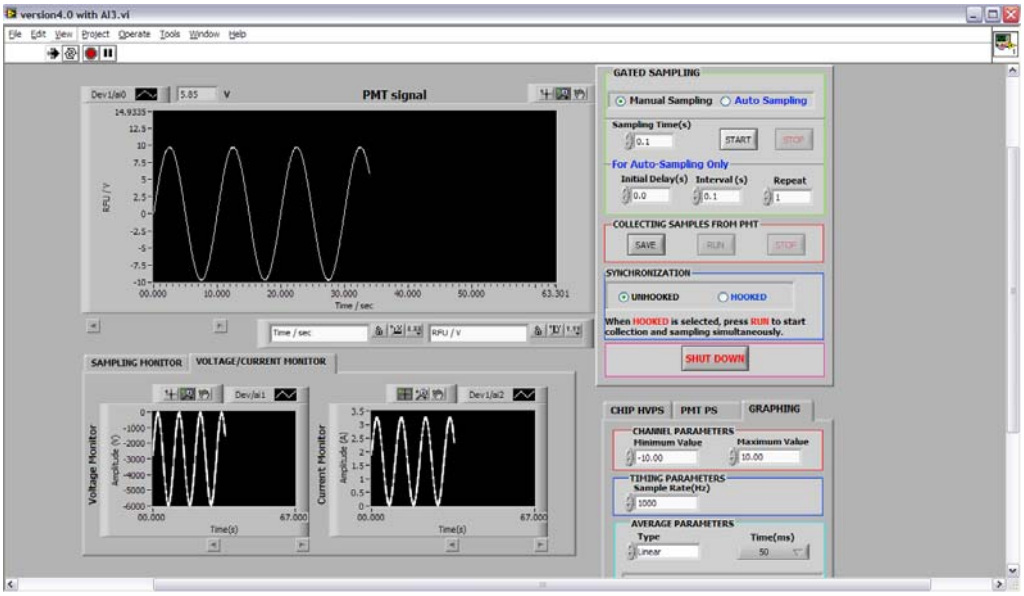

Figure 14. Screenshot of the front panel in the control program

2.4 SYSTEM TESTING AND PRELIMINARY EXPERIMENTS

2.4.1 Beam alignment

The beam alignment starts when the stage A, B and tower C with optical components are installed together as in Figure 12. A plain glass slide (25 mm x 75 mm, 1mm thickness) with a fluorescent label stick to one side is used to assist the alignment of the excitation laser beam. The glass slide is first lay on the stage A right above the aperture in the middle. After turn on the power supply for the laser, the beam is reflected 90 degree by the dichroic filter towards the objective and formed a bright fluorescent spot on side of the glass slide with the fluorescent label. The diameter of the spot becomes larger when as the slide is moved little away from the objective by elevating the stage A. Meanwhile, the shape of the spot can be distinguished easily.

Three thumbscrews on the beam steering mirror holder supporting the dichroic mirror are adjusted so that the shape of the spot is round. Eclipsed spot appears when the beam is hitting the inner barrel of the objective lens, which should be avoided.

After the excitation beam is aligned, the glass slide is replaced by a simple test microfluidic chip as shown in Figure 15. The bottom glass of the chip has a thickness of 1.00 mm. The diameter and the depth of the big round reservoir on the chip are about 6.72 mm and 1.80 mm, respectively. The depth of the channel on the chip is around 20 μm. About 50 μL of newly prepared solution of Thioglo 1 (0.5 μM) and GSH solution (0.1 μM) is loaded into the reservoir. A piece of fluorescent label is placed on the rail about 10cm away from the center of the tower with its face towards the front surface mirror. The height of the stage A is then roughly lower so that the laser beam is focused onto the middle of the solution. At the same time, a more tightly focused spot can be observed on the fluorescent label. When the focused spot (≈ 1 mm ID) is much brighter than its background, the thumbscrews for the dichroic filter is finely adjusted so that three distinguished spots appear on the fluorescent label and are clearly separated from each other. Among them, two spots are the images formed by the laser beam reflected by the objective and the bottom glass of the microfluidic chip. And only one of them is the true image of the fluorescence signal from the sample. The real signal image can be distinguished from the other two by changing the fluorescent label into a white one. The image formed by the fluorescence signal has a unique color close to cyan, while the other two images formed by the reflection light have the color close to indigo just like the color of the laser beam. A noisy optical background would exist if the image of the fluorescence signal overlaps the image of the reflection light.

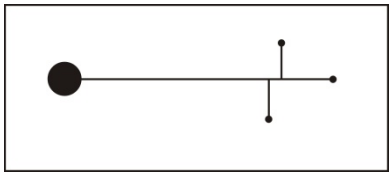

Figure 15. Sketch of the simple test microfluidic chip

In order to make sure the focused beam is in parallel with the rail, two iris diaphragms with the minimum aperture diameter of 1mm are used to ease the parallel alignment. A sketch of the setup is presented in Figure 16. The emission filter is temporarily removed from stage C and placed before the front surface mirror. The iris diaphragm A is placed at 10 cm away from the center of the front surface mirror. Iris diaphragm B is parallel with A and the distance between them is about 2.5 cm. The height of diaphragm A and B are carefully adjusted so that the distance between the center of the aperture and the rail is equal to that of the pinhole on stage C and the rail. A fluorescent label is firstly placed between the iris diaphragm A and B. Three thumbscrews on the beam steering holder for front surface mirror are finely adjusted, so that a spot is formed on the label. After that, the label is removed and placed after iris diaphragm B. The angle of the mirror is further adjusted so that the focused beam passes through the second diaphragm and forms a spot on the label.

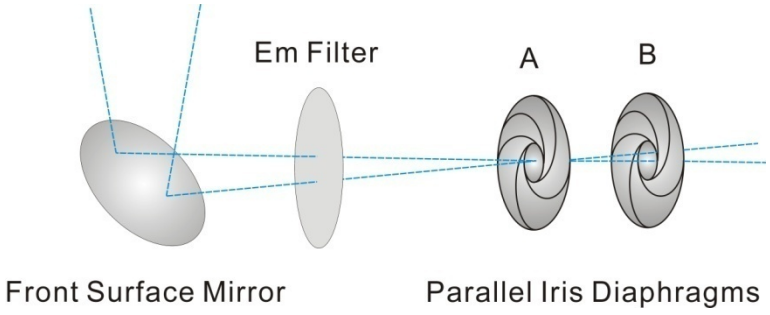

Figure 16. Set up of two parallel iris diaphragms in parallel alignment

After the focused beam is aligned parallel with the rail, the stage C with 400 μm pinhole, emission filter and PMT is fixed on the rail. The position of the pinhole is finely adjusted with its micro driver, so that the focused beam is aimed at the center of the aperture. After turn on the control program and power supply for PMT, signals can be read from the chart on the front panel when a proper control voltage is selected. The micro drivers of the translation stage and the pinhole are finely tuned until a maximum signal is presented on the chart.

2.4.2 Laser beam profile measurement

In the confocal LIF system, the laser beam is focused by the objective onto the sample in the channel, thus it is useful to have a full picture of the intensity profile of the focused laser beam in order to optimize the dimension of the channel and other related parameters. Ideally, laser beam can be depicted as a Gaussian intensity profile, which corresponds to the theoretical TEM_{00} mode. However, when output of the real-life laser beam is concerned, a beam quality factor, M^2, has come into general use. In the following experiment, a simple method is presented for measuring the laser beam intensity profile. The result is further compared with that got from theoretical calculation.

The set up used in the laser beam profile experiment is shown in Figure 17. A thin blade with a small aperture in its center is bonded to a plain glass slide with a thickness of 1.00 mm. The collar ring on the 40x LUCPLFLN objective is adjusted to the corresponding position for cover glass thickness compensation. The stage A is temporarily removed and the holder is fixed on the heavy duty rod, so that the aperture on the blade is directly above the objective. A low power detector (818-UV, Newport, Irvine CA) with an active diameter of 1.13 cm is also fixed on the rod at a height just above the blade with its active surface facing the aperture on the blade.

The adjustment factor for the power meter (1815-C, Newport, Irvine CA) connected to the detector is set to be 3.81×10^3 W/A for 400 nm wavelength measurements. The distance between the detector and the objective is fixed to be about 2.8 cm.

At the beginning of each run, the height of the glass slide is slowly decreased until the bottom of the glass is just in touch with the surface of the pupil lens on the objective. The absolute height is then read from the micro driver on the z-axis linear stage. The glass slide is again lift up ~ 2 mm above the objective. The actual distance, D_Z (z is the propagating direction of the focused laser beam), can be calculated from the difference between readings of the micro driver at different heights. When the height of the glass slide is fixed, the y-axis linear stage is adjusted so that the laser beam passes through the center of the aperture on the blade. After that, the micro driver on the x-axis is turned to a position where the laser beam is fully blocked by one side of the blade and the reading on the power meter indicates 0.00 mW. The x-axis driver is turned back slowly step by step afterwards until the reading on the power meter reaches its maximum. Readings of the power meter and the micro driver from each step are recorded for further analysis. The whole processes are repeated when the glass slide changes to other height in z-axis.

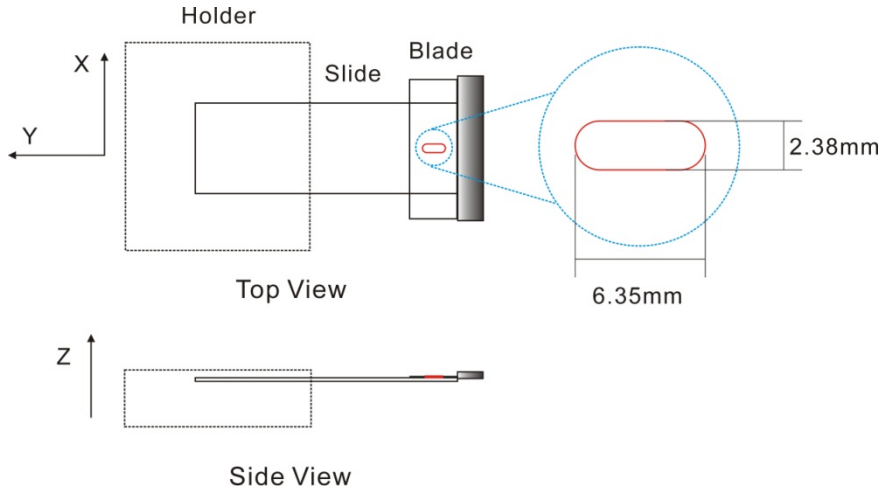

Figure 17. Set up for profile measurement of the laser beam

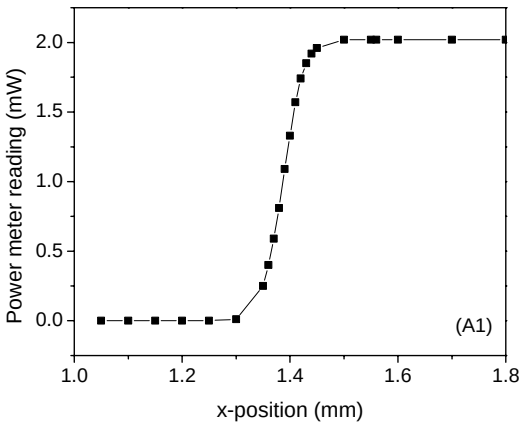
Power meter reading (mW)
x-position (mm)
(A1)

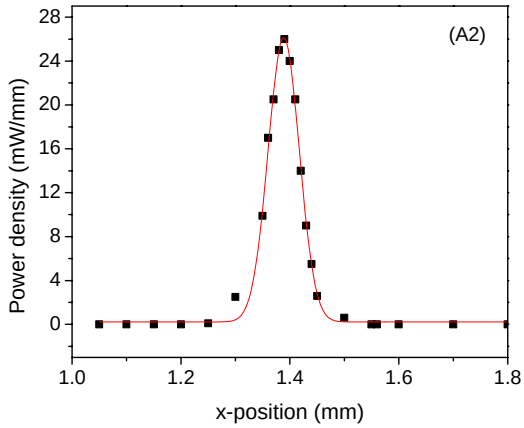
Power density (mW/mm)
x-position (mm)
(A2)

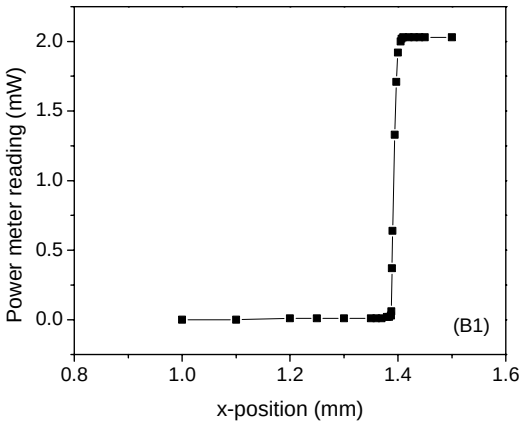
Power meter reading (mW)
x-position (mm)
(B1)

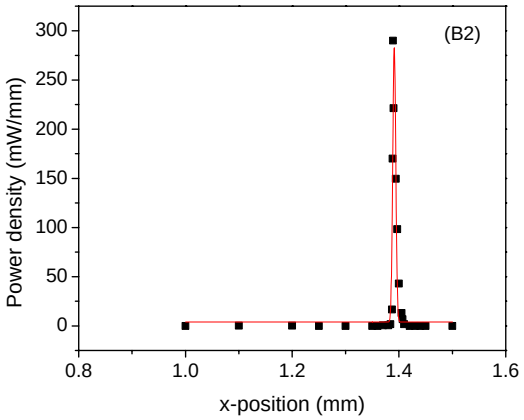
Power density (mW/mm)
x-position (mm)
(B2)

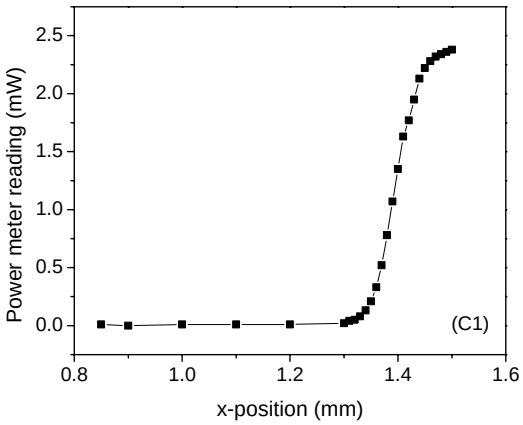
Power meter reading (mW)
x-position (mm)
(C1)

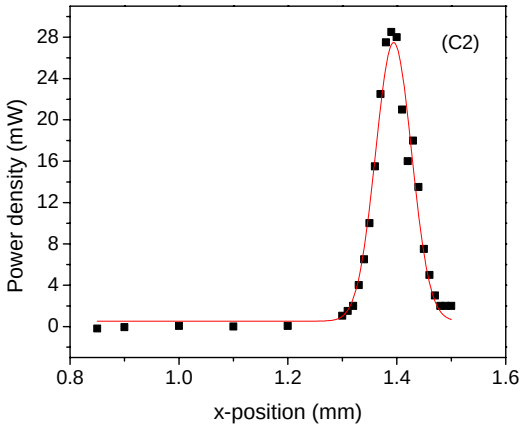
Power density (mW)
x-position (mm)
(C2)

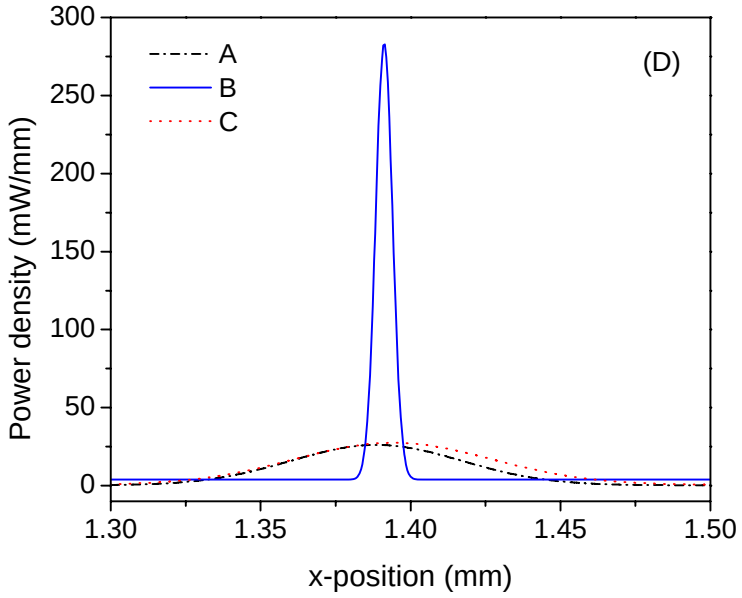

Figure 18. Results from laser beam profile measurements at different W. D. (A1) 2.507 mm; (B1) 3.250 mm; (C1) 4.030 mm; The results are then differentiated and fitted to Gaussian distribution and plotted in A2, B2, C2, respectively. Three Gauss fits are plotted together in plot D for comparison.

Table 9. Gaussian fitting results for three measurements

Run #	D_Z (mm)	Area (mW)	Center (mm)	Width (mm)	Offset (mW/mm)	Height (mW/mm)	R^2
A	2.507	1.85	1.389	0.057	0.223	25.9	0.973
B	3.250	1.97	1.391	0.006	3.84	280	0.867
C	4.030	2.24	1.394	0.066	0.528	27.0	0.996

The relationship between the laser power and x-axis positions from three runs with different D_Z, (2.507 mm (A1), 3.250 mm (B1), 4.030 mm (C1)) are plotted in Figure 18. Each step in our experiment along the x-axis can be treated as a definite integration of the laser beam power not blocked by the blade from the start point to current position on x-axis. These results are then differentiated and fitted to Gaussian distribution according to Eq. 8.

$$y = y_0 + \frac{A}{w \cdot \sqrt{\pi/2}} \cdot e^{-2 \cdot (\frac{x - x_c}{w})^2} \tag{8}$$

Where y_0, x_c, w and A are the offset, center, width and area of the Gaussian distribution, respectively. When the laser beam is concerned, these four values represent the offset for the power density, beam center, beam width (radius of the $1/e^2$ irradiance contour) and total beam power, correspondingly. The fitting constants for three runs are listed in Table 9. It is obvious from the Figure 18 that the power density (mW per mm) of the laser beam in run B is much larger than that in run A or C. The D_Z. in run B is 3.250 mm, which falls into the listed W.D. range of this objective.

When Gaussian beam propagates through a simple lens, the output beam will still have a Gaussian intensity profile. Therefore, it is reasonable to fit our results by using the propagation equation for a real laser beam. The radius of the $1/e^2$ contour after the real wave has propagated a distance z, $w_R(z)$, can be expressed by Eq. 9

$$w_R(z) = w_{0R}\left[1 + \left(\frac{z\lambda M^2}{\pi w_{0R}^2}\right)^2\right]^{1/2} \tag{9}$$

Where z is the distance propagated from the plane where the wave front is flat, or the location of a Gaussian waist; λ is the wavelength of the beam; w_{0R} is the radius of the $1/e^2$ irradiance contour of a real beam at the beam waist. The results from non-linear curve fit are given in Figure 19 and Table 10.

We used D_Z in the non linear curve fit instead of z as in Eq.9. This indicates that the beam waist will locate at the front surface of the slide glass when the distance between the bottom of the glass slide and the surface of the pupil lens on the objective equals to D_{Z0}. Table 10 presents two important parameters obtained from non-linear curve fit. One is the radius of the beam waist, w_{0R}, which is around 2 μm. The other is the W.D. of this objective with a 1 mm thick glass slide,

D_{Z0}, which is 3.205 mm (Strictly speaking, W.D. ≠ D_{Z0}, but they are very close to each other in our case.)

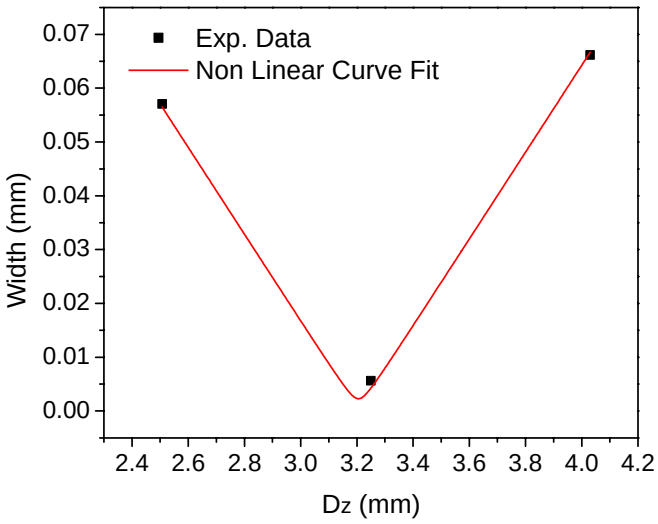

Figure 19. Plot results from non linear curve fitting of the beam width and D_Z

Table 10. Equations and parameters for non linear curve fitting of the beam width and D_Z

$w_R(D_z) = w_{0R}\left[1+\left(\frac{(D_Z - D_{Z0})\lambda M^2}{\pi w_{0R}^2}\right)^2\right]^{1/2}$						
Constant		$\lambda = 403.1 \times 10^{-6}$ mm				
		$M^2=1.2$				
Dependent Variable		W_R (width of the Gaussian distribution from Table 9)				
Independent Variable		D_Z (see Table 9)				
Results	Parameters	w_{0R} (μm)	Value	2	Error	0.04
		D_{Z0} (mm)		3.205		0.01
	R^2	0.99887				

Meanwhile, it is possible to calculate the radius and the location of the beam waist after a spherical Gaussian beam passes through a trains of lenses by using approaches and formulas

developed by S. A. Self in 1983.[141] If the waist of the input beam represents the objective and the waist of the output beam, represents the image, the relationship between image distance, s″, and the objective distance, s, is given by Eq. 10, under paraxial conditions:

$$\frac{1}{s+\left(z_R/M^2\right)^2/(s-f)}+\frac{1}{s''}=\frac{1}{f} \tag{10}$$

where z_R is the Rayleigh range of the input beam defined by Eq.11

$$z_R=\frac{\pi w_{0R}^2}{\lambda} \tag{11}$$

The magnification, m, is given by

$$m=\frac{w_{0R}''}{w_{0R}}=\frac{1}{\sqrt{\left\{\left[1-(s/f)\right]^2+\left[(z_R/M^2)/f\right]^2\right\}}} \tag{12}$$

Where w_{0R}'' is the radius of the beam waist on the image side.

In most cases, the beam waist is designed to be very close to the output surface of the laser. Therefore we can assume that the w_0 is 0.5 mm and s is ≈130 mm for our setup. The focal length for 40x objective is 4.500 mm. s″ and w_{0R}''calculated from Eq. 10, 11, 12 are 4.501 mm and 1 μm, respectively, which indicates that the waist of the output beam is not exact at the focal plane of the objective, but 1 μm away. However, the radius of the beam at the focal plane is only 0.28% larger than the beam waist. The results from the beam profile experiments are consistent with what we got from the theoretical calculation.

2.4.3 Noise experiment and system testing

2.4.3.1 Noise sources

Identification of the dominant noise sources is of vital importance for optimizing experimental variables systematically and modifying the instrumental design to get a better SNR. The total noise observed in a measurement may arise from several sources, among which one or two noise sources often dominate.

For a photoluminescence measurement, the total signal, E_t, equals to the summation of the analytical signal E_s and the blank signal E_{bk}, where E_{bk} includes contributions from the background signal, the dark signal, and offsets from the signal processor system. Similarly, the RMS noise in the total signal, σ_t, has contributions from analytical signal (σ_s) and the blank signals (σ_{bk}). σ_S is mainly due to analytical signal shot noise, $(\sigma_S)_s$ and flicker noise $(\sigma_S)_f$. σ_{bk} is originated from noise in the background signal, σ_B, and the total dark current noise, σ_{dt}. Furthermore, σ_B can be divided into background signal shot RMS noise, $(\sigma_B)_s$ and flicker RMS noise $(\sigma_B)_f$. On the other hand, σ_{dt} includes the actual noise in the dark current, σ_d, and the amplifier-readout noise, σ_{ar}. Finally, σ_d includes the dark current RMS shot noise, $(\sigma_d)_s$, and the excess rms noise, $(\sigma_d)_{ex}$. The RMS noise from different sources can be added up quadratically if all of them are assumed to be totally uncorrelated. The affiliation among all these various noise sources is summarized in Figure 20. It can be concluded from Figure 20 that there are three primary noises sources existing in the analog signal processing: the noise in the analytical signal, the noise in the background signal, and the noise from the dark current and amplifier-readout system.

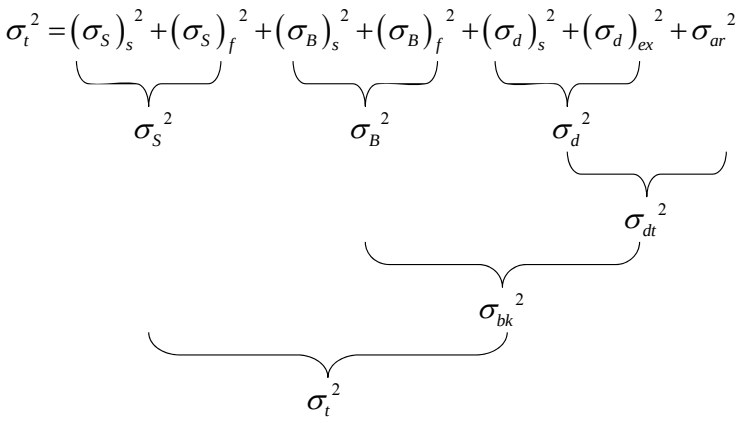

Figure 20. Structure plot of the relationship between different RMS noises for an emission measurement

SNR is an important parameter in testing the performance of the system, which contains the RMS noise. Mathematically, it can be expressed as

$$\frac{S}{N} = \frac{E_S}{\sigma_t} \tag{13}$$

For our confocal LIF system, the main sources of $(\sigma_S)_s$ are the quantum noise and PMT multiplication noise. $(\sigma_S)_f$ is mainly due to the variation in laser radiance resulted from the fluctuation in the electrical power, temperature or vibrations. Besides, the vibration of the whole setup, especially the sample stage also contributes to the flicker noise in analytical signal. σ_B mainly comes from background scattering and luminescence, such as the scattering light from the wall of the microchannel, light from computer monitor or any other light source in the room. It is worth to notice that laser flicker noise is also related with σ_B, as the scattering signals are all proportional to the excitation source radiant power and suffer an equivalent fluctuation due to source flicker. σ_{dt} is relatively weak compared with other noises mentioned according to its listed value.

2.4.3.2 Identification of different noise sources

Several experiments were designed to test the RMS noises from different sources for identifying the dominant one(s) in the system.

The first experiment is mainly designed to test the environmental noises such as the scattered light from computer monitor and a weak ceiling lamp. The laser power is set to be 3.0 mW and PMT control voltage is 0.556 V. No cover glass is placed on the sample stage. The sampling rate is 10 Hz. A 20x objective is used in the system. The results of this experiment are summarized in Table 11.

Table 11. Environmental noises testing*1

Parameters	Computer Monitor Only	Ceiling Lamp Only	Computer Monitor & Ceiling Lamp	No Monitor or Ceiling Lamp
σ (mV)	2.460	2.165	3.338	0.428
E_{bk} (mV)	0.494	7.578	8.674	0.206

*1 laser power is 3.0 mW; PMT control voltage is 0.556 V; 20x objective; Sampling rate is 10 Hz; No cover glass on the stage; sample is not loaded; no light tight cover over the stage C.

It is indicated by the Table 11 that the main noises in this experiment come from background scattering and luminescence of the computer monitor and ceiling lamp. The signal and noise contributed by the dark current and amplifier readout are very small, because the signal and RMS noise for the system are only 0.000206 V and 0.000428 V, respectively. As the noise from the computer monitor, σ_c, ceiling lamp, σ_l, and total dark current noise, σ_{td}, are independent, they can be added quadratically as follows:

$$\sigma_t = \sqrt{\sigma_c^{\,2} + \sigma_l^{\,2} + \sigma_{td}^{\,2}} \qquad (14)$$

The calculated RMS noises for different sources and their contribution (%) are listed in Table 12. The total RMS noise and the blank signal are also compared with those obtained from previous experiments. It is obvious that ceiling lamp contributes 93.7% of the background signal. Meanwhile noises from computer monitor and ceiling lamp account for 55.6% and 42.7% of the total noises, respectively. It is wise to turn off the ceiling lamp and have a light tight cover over the stage C during the experiments to block and reduce these background noises.

Table 12. RMS noise from different background sources

Parameters	Computer Monitor (Calc.)	Ceiling Lamp (Calc.)	Total Dark Current (Expt.)	Summation	
				Calc. *1	Expt. *2
σ (mV)	2.422	2.122	0.428	3.248	3.338
(%)	(55.6)	(42.7)	(1.74)		
E_{bk} (mV)	0.288	7.372	0.206	7.866	8.674
(%)	(3.66)	(93.7)	(2.62)		

*1 Obtained by adding the values in the first three columns.

*2 Obtained from Table 11 under the conditions when computer monitor and ceiling lamp are both on.

The following experiment is designed to study the noise from the scattered and reflected light from the cover glass. Most of the basic parameters of this experiment are same with that in the first experiment, except that a cover glass of 1mm thickness is placed on the sample stage and the laser power is increase to 7.4 mW. Ceiling lamp is kept off for all the experiments discussed below. The total signal and RMS noise are summarized in Table 13 for both cases when computer monitor is turned on and off.

Compared with σ_{dt} in the first experiment, the result in the scattering experiment when computer monitor is off shows a little increase in its value. The most possible explanation for this is that the system in the scattering experiment has one additional source of noise, which is

the scattered and reflected light from the cover glass. Assuming that σ_{dt} is same for both experiments, the contribution of signal and noise from the scattered light are about 0.000279 V and 0.000505 V, respectively, which are relatively weak compared with the noise from the computer monitor and ceiling lamp.

Table 13. Results of the scattering experiment [*1]

Parameters	Computer monitor	
	On	off
σ (mV)	2.448	0.662
E_{bk} (mV)	0.189	0.485

*1 laser power is 7.4 mW; PMT control voltage is 0.556 V; 20x objective; Sampling rate is 10Hz; with cover glass on the stage; sample is not loaded; ceiling lamp is off, no light tight cover over the stage C.

In the third experiment, the laser head and PMT are temporarily removed from the system and lined up with several neutral density filters between them. The heights of the PMT and laser are adjusted so that laser beam is just aimed at the active surface of the PMT. The goal of this experiment is to test the noise contributed by the laser and PMT together. The RMS noise is obtained when the ceiling lamp and computer monitor turned off. Results and main parameters of this experiment are listed in Table 14.

Table 14. Laser beam and PMT stability analysis[*1]

Run #	Laser Power(mW)	PMT Control Voltage (V)	Neutral Density Filter (OD)	σ (V)	E_t (V)
1	3.00	0.375	4	0.014	5.861
2	10.0	0.375	5	0.007	1.538
3	15.0	0.375	5	0.008	2.418

*1 Sampling rate 10Hz; ceiling lamp and computer monitor are both off.

It can be seen from Table 14 that the total RMS noise from PMT and laser is enhanced when the analytical signal increases. The noise sources from this experiment mainly come from flicker noise of the laser, shot noise due both to quantum noise and PMT multiplication noise. Total dark noise only accounts a small portion (≈ 0.3%) of the total noise. Linear fitting results in Figure 21 indicates that SNR is proportional to $(Es)^{0.46}$, which further proves that the shot noise contributes a lot to the total noise because the exponent is close to 1/2.

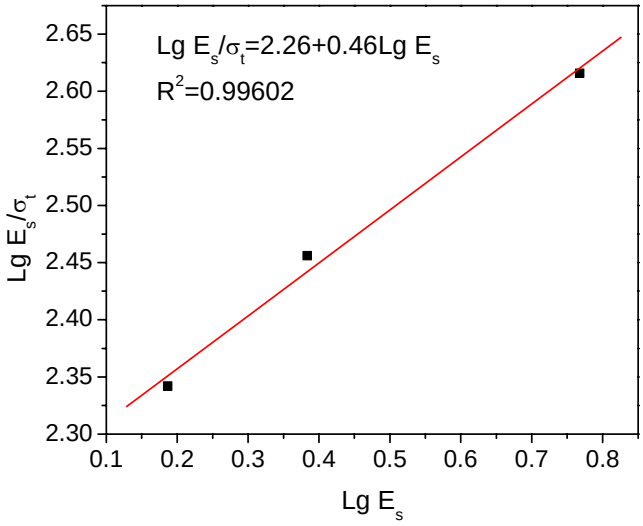

Figure 21. Linear fitting of the results from laser and PMT stability experiments.

Finally, the real sample is tested when there is a light tight cover over the stage C. The ceiling lamp is kept off throughout the experiment. The computer monitor is not turned off, because it is necessary to be on for monitoring and controlling. A 40x objective is installed in the system. Newly prepared sample solution, which contains 0.50 mM Thioglo 1 and 0.10 mM GSH, is loaded into the large reservoir on microfluidic chip shown in Figure 15. The level of the stage A is finely adjusted so that the laser beam is focused onto the solution in the reservoir. PMT

control voltage is set to be 0.5 V and the laser power is fixed at 3.0 mW. The total RMS noise is 0.047 V, while the total signal level is 5.449 V. Figure 22 is a picture of microfluidic chip with sample in reservoir taken during the experiment. Compared with the RMS noise in the previous experiment, it is obvious that analytical signal shot noise and flicker noise account for a large percentage of the total noise.

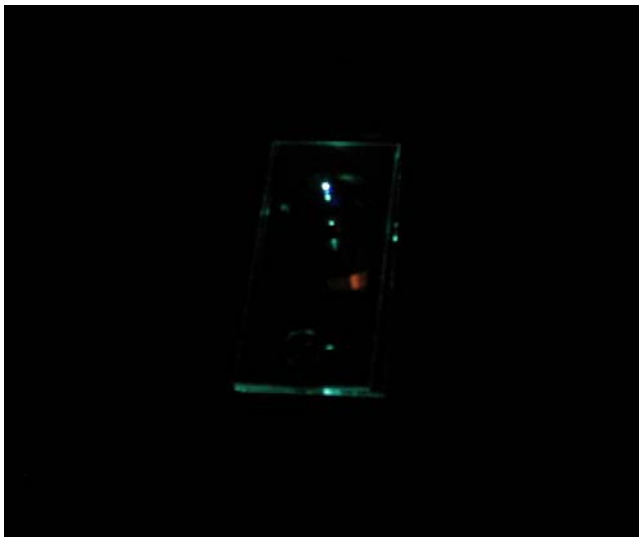

Figure 22. A photo of the microfluidic chip in one experiment.

2.4.3.3 Noise reduction by averaging and low pass filter

Two methods were applied to help reducing the noise in our system, averaging and low pass filter. The premise of reducing noise by averaging multiple samples is that noise and measurement error is random, and therefore, by the central limit theorem, the error will have a Gaussian distribution. By averaging multiple points, you can get a mean that is statistically close to the actual value. Besides, the standard deviation derived from the measurements indicates the width of the normal distribution around the mean, which describe the probability density for the location of the actual value. Further more the standard deviation of the average of the samples

(σ_{avg}) is reduced from the standard deviation of each individual sample (σ) by a factor of $1/\sqrt{N}$, where N is the number of points used in the averaging. Therefore, the more points averaged, the closer you know the actual value.

When applying averaging in experiments, it is necessary to pay attention to some practical limits, such as the sample clock rate of the DAQ device, the processor's speed, buffer size. Besides, all samples taken for averaging should come from a range of time where the real signal varies little in amplitude compared with the error that you are trying to eliminate. In other words, it is necessary to know the maximum frequency component of a signal. In our system, the resolution is acceptable when using a sampling rate of 100Hz for a peak with a maximum FWHM of 0.1 s. If we set the sample clock rate of the DAQ device to be 10000 Hz and the averaging time to be 10ms, the temporal resolution for the system will remain to be 10ms (100 Hz), while the number of averaged points in one period will be 100 and the standard deviation will decrease to 1/10 of its original value.

Averaging is simply achieved by using "averaging function" in control program. The averaging time is fixed to be 50ms, but the sample clock rate is changed from 20, 100, 1000, 10000 and 100000 Hz. In this case, the temporal resolution is maintained at a same level for all the experiments while different numbers of points, n, are averaged. PMT control voltage is adjusted to be 0.5V and the laser power is set to be 3.0 mW. Sample solutions, which contains 0.50mM Thioglo 1 and 0.10mM GSH, is introduced into the microchannel on microfluidic chip shown in Figure 15 by applying vacuum at the other end of the channel. A 40x objective is used to focus the laser beam into the center of the channel. The results are shown in Table 15 and Figure 23.

Table 15. Results of averaging[*1]

	Sample Clock Rate	Averaged Points	E_t (V)	σ_t(V)
Sample (0.50mM Thioglo 1 and 0.10mM GSH)	20	1	5.143	0.221
	100	5	5.156	0.069
	1000	50	5.146	0.026
	10000	500	5.133	0.024
	100000	5000	5.126	0.026
Base Line	1000	50	3.578×10^{-4}	5.66×10^{-5}

*1 laser power is 3.0 mW; PMT control voltage is 0.500 V; 40x objective; averaging time is 50 ms (sampling rate 20 Hz); light tight cover over the stage C.

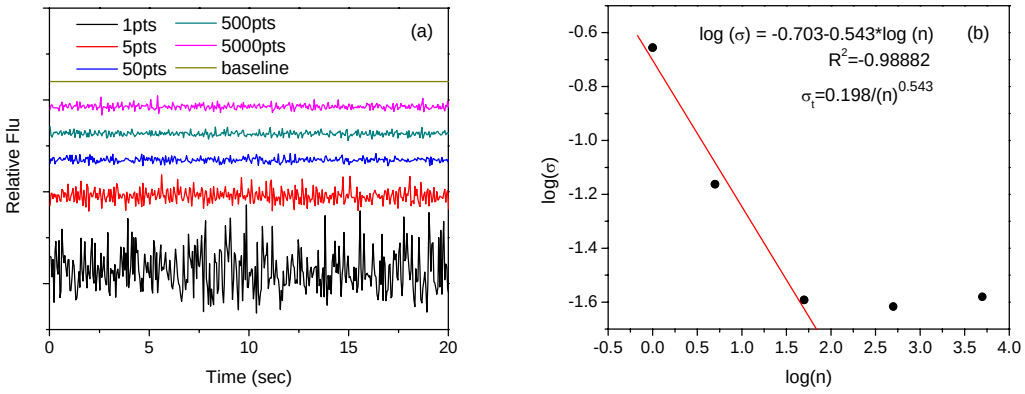

Figure 23. Results from different averaged points (a) and linear fitting of the 1, 5 and 50 points averaging treatment (b).

The linear regression indicates that the total RMS noise level, σ_t, is kept decreasing as the number of averaged points, n, is increasing within a certain range (0-50 points). σ_t is proportional to $1/ (n)^{0.543}$, which is consistent with what is predicted by the theory. However, this trend stops after the number of averaged points reaches a certain level, which is ~50 in our case. This phenomenon implies that there are some noise sources with certain frequencies in our system, as averaging is only good for random noise with Gaussian distribution.

The function of a low pass filter is to block the aliases resulted from the noise with high frequency. Aliasing exists when the frequency of a signal or noise is higher than the Nyquist frequency, which is defined as half the sampling frequency or the cut-off frequency of a sampling system. When aliasing happens, the low frequency aliases of the under sampled high frequencies will appears in the system, which either results in a false frequency of the signal or a noisy background.

The alias frequency $f_a(N)$ of a signal or noise with high frequency equals to the minimum absolute value of the difference between the frequency of the input signal, f, and the closest integer multiple of the sampling rate, $N \cdot f_s$, as given by Eq. 13

$$f_a(N) = \left| f - N \cdot f_s \right|_{\min} \tag{13}$$

It can be deduced from the above equation that signal must be sampled at a rate no less than twice the highest frequency component of interest in the signal ($f_s>2f$) in order to capture the highest frequency component of interest; otherwise, the high-frequency content will alias at a false lower frequency in the sample data. In practice, the sampling rate must be set high enough (about 5 to 10 times the highest frequency components in the signal) to obtain accurate measurements using sampled data. Besides, in real world signals often contain noise with frequency higher than the Nyquist frequency. These frequencies are erroneously aliased and added to the components of the signal that are sampled accurately, producing distorted sampled data. Therefore a low pass filter, that attenuates any unwanted frequencies in the input signal that are greater than the Nyquist frequency, must be introduced before the analog to digital convertor (ADC) to restrict the bandwidth of the input signal to meet the sampling criteria.

A Wavetek 852 dual Hi/Lo variable filter (Willtek, Germany) is added between the signal output end of PMT and DAQ device. Newly prepared sample, which contains 0.50mM Thioglo 1

and 0.10mM GSH, is loaded into the large reservoir on microfluidic chip shown in Figure 15. The sampling rate is kept at 1000 Hz through out the experiment. The cut off frequency of the filter is changed from 0 Hz to 5000 Hz. Under each specific frequency, the experiment is repeated for 10 runs and each lasts for ~15 s. Before using with Fast Fourier Transform (FFT) to extract the character frequency of the noise, we treated all data sets with the methods described by Morgan and Weber.[142] Briefly, a smoothed curve is obtained for each run by using adjacent averaging. This smoothed curve is then subtracted from each original curve, respectively. The resulted data sets are finally averaged and treated with FFT. The results after adding a low pass filter is summarized in Table 16 and Figure 24. It can be seen from the data that the analytical signal obtained is accompanied by noises with several characteristic frequencies around 20 Hz, 30 Hz, 45 Hz and 60 Hz. When the cutoff frequency of the low pass filter is decreased, noise with frequencies higher than the cut-off frequency disappears and the total RMS noise level went down, too. Besides, the frequencies of the noise are concentrated below 100 Hz, therefore when the cut off frequency is higher than 100 Hz, the low pass filter has no obvious effect for decreasing the total RMS noise.

Table 16. Results from low pass filter testing[*1,*2]

Cut Off Freq.(Hz)	E_t	σ_t
0	5.449	0.047
5	5.313	0.006
50	5.530	0.035
500	5.548	0.033
5000	5.520	0.035

*1 laser power is 3.0 mW; PMT control voltage is 0.500 V; 40x objective; Sampling rate is 1000 Hz; light tight cover over the stage C.

*2 Only one channel of the variable filter is used; 0 dB gain; flat amplitude

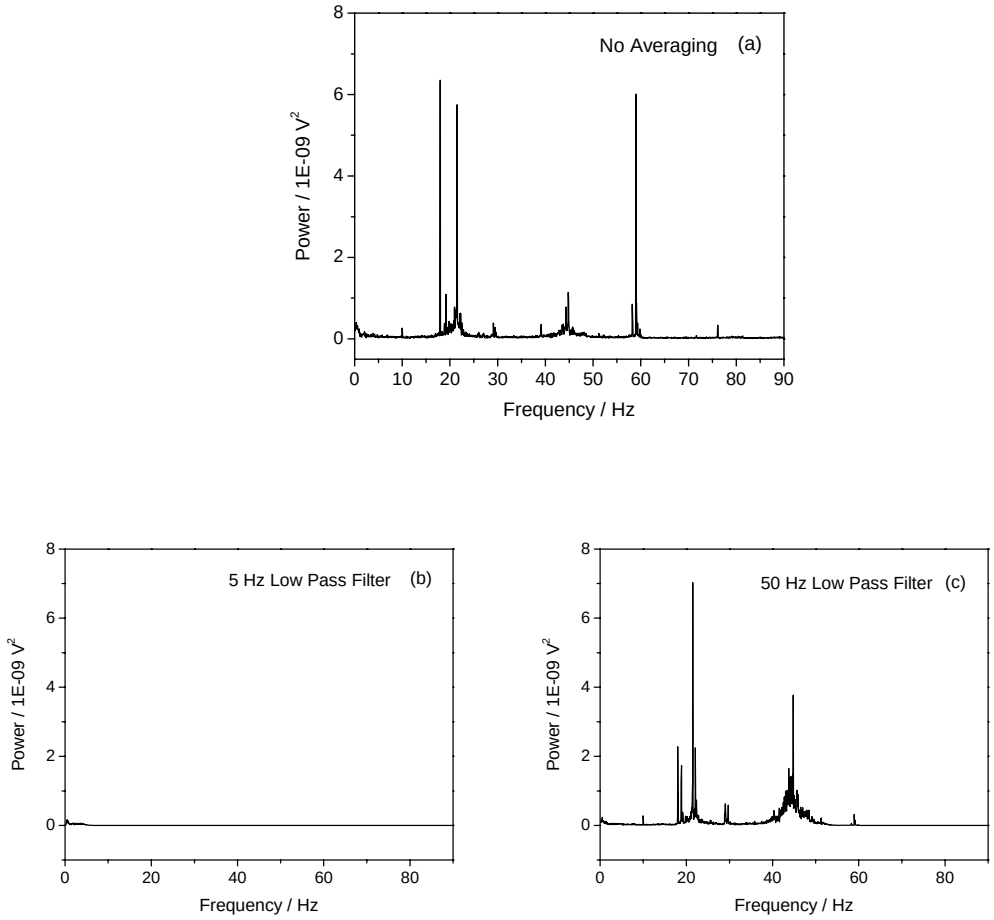

Figure 24. FFT of the results from low pass filter with different cutoff frequency, (a) no filter; (b) 5 Hz; (c) 50 Hz.

Further experiments proved that these noises with certain frequencies are mainly caused the vibration of the system. In these experiments, we added four racquetballs under the optical breadboard and a rubber layer between the platform and linear stages in stage A to damp the transference of the vibration from bench to sample stage. According to the results (see Table 17 and Figure 25), there is a distinguishable change in the noise intensity, which implies that the sources for these noise are closely related with vibration.

Table 17. Results from racquetball testing[*1,*2]

Racquetballs	E_t	σ_t
Yes	6.712	0.023
No	6.586	0.048

*1 laser power is 3.0 mW; PMT control voltage is 0.400 V; 40x objective; Sampling rate is 1000 Hz; light tight cover over the stage C.

*2 Sample contains 0.50 mM Thioglo 1 and 0.10 mM GSH and is loaded in the large reservoir of the microfluidic chip shown in Figure 15.

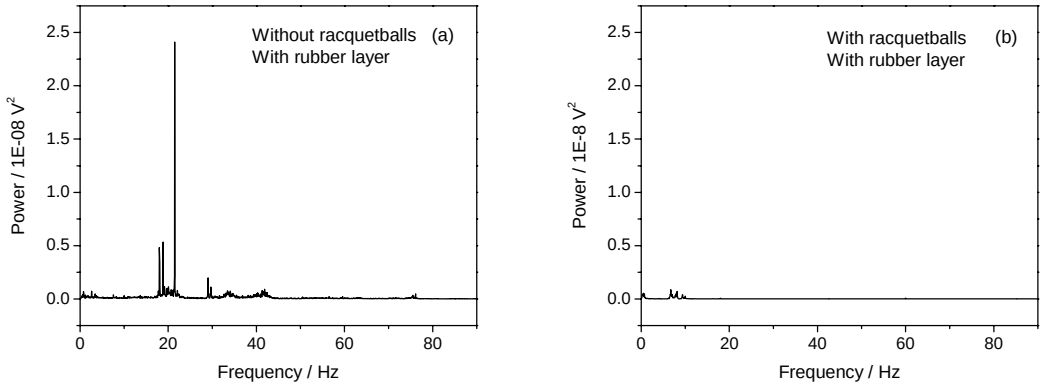

Figure 25. Results from different averaged points (a) and linear fitting of the 1, 5 and 50 points averaging treatment (b).

2.4.3.4 System testing

Several experiments are designed to test the performance of the detection system, which includes the relationship between fluorescence responses and PMT control voltage/laser power; linearity of the system with change in concentration. In PMT control voltage experiment, sample solution, which contains 50 μM Thioglo 1 and 10.7 μM GSH, was loaded into the large reservoir on microfluidic chip in Figure 15. The averaging time is set to be 50 ms when the sample clock rate is 1000 Hz. The cutoff frequency of the low pass filter is adjusted to 10 Hz. The laser beam

with a power of 3.0 mW is focused on the sample with a 40x objective. The results are shown in Figure 26 (a). It is interesting to notice that there is an optimized range where the ratio of E_t and σ_t arrives its highest level, which is useful for selecting a proper PMT control voltage. The experiment conditions in laser power experiment are similar to those in PMT control voltage experiment, except that the control voltage for PMT is fixed at 0.5 V while laser power varies in different runs. The results are ploted in Figure 26(b), which indicates that when the sample has a fixed concentration, the fluorescence response is not increasing without any bound when the power of the laser beam is enhanced. This is mostly because the optical saturation of the absorbance transition for the dye will finally be obtained under a high irradiance of the beam. A significant fraction of the analyte will be raised to the excited state and the number of photons absorbed per second approaches the spontaneous emission rate under the first approximation. The increase in the laser power after saturation will only lead to photodegradation of the dye.

Sample solution with different concentration of Thioglo 1 and GSH are also used to test the linearity of the system. All other conditions are same as the previous experiment unless otherwise specified. Results from linearity experiments are plotted in Figure 27. Due to the limitation of the PMT, the linear range for GSH ([GSH]: [Thioglo1]=1:5) spans from 0-49.7 μM. The detection limit is calculated as follows:

$$LOD = \frac{3 \cdot \sigma_{bk}}{Slope} = \frac{3 \cdot 4.42 \times 10^{-5}}{0.09151} = 1.45 \text{ nM}$$

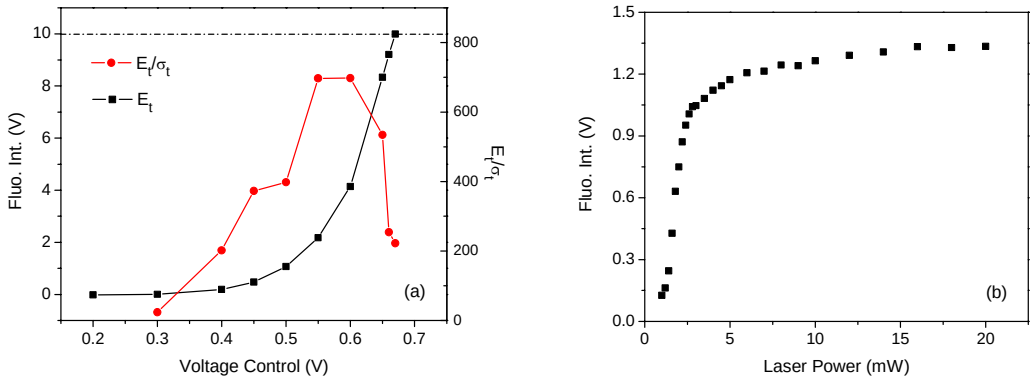

Figure 26. Relationship between the fluorescence intensity and PMT control voltage (a) and laser power (b).

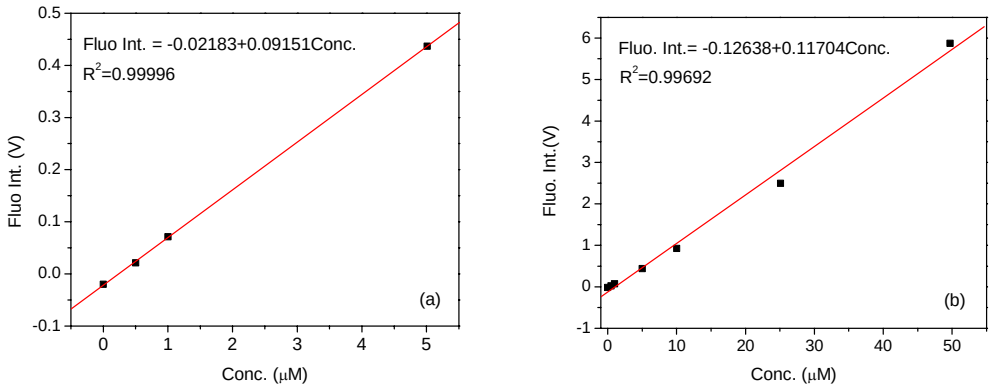

Figure 27. Results from the linearity experiment. (a) 0-5.01 μM; (b) 0-49.7 μM.

2.4.4 Reaction between Thioglo 1 and GSH

Thioglo 1 (see Figure 28) is used as a fluorescent thiol reagent in determination of the GSH. Thioglo reagent is a kind of maleimide derivatives of naphtthopyranone fluorophores. Compared with other widely used dyes mentioned in Section 1.2.2., Thioglo reagents have several advantages. Firstly, they have very low quantum yield before reacting, therefore it is not

necessary to separate the unreacted dye with the bounded dyes before any detection is performed; secondly, the quantum yield of the conjugates of Thioglo and GSH is very high, which is good for detecting samples with low concentration; thirdly, the hydrolysis rate of the Thioglo reagent and GSH is slower than most other maleimide reagent. Besides, the stock solution of this reagent is very stable and its hydrolyzed products are all inactive with thiol ground and have low quantum yield; last but not least, the reaction between Thioglo and GSH only takes seconds in buffered system at pH7.0.

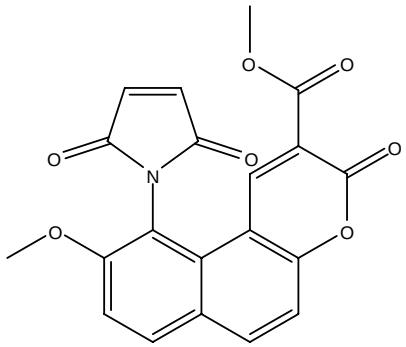

Figure 28. Structure of Thioglo 1.

The pH effect on the reaction rate between Thiolgo 1 and GSH is studied in the following experiments. A series of solutions (29.7 μM GSH, 15 μM Thioglo 1, 50.1 mM Tris-Acetate buffer solution) with various pH values, ranging from 4 to 9, are measured with a commercial fluorescence device (Spectra Max M2, Molecular Devices, Sunnyvale, CA). The measurement is taken right after the solutions are made. The results are plotted in Figure 29. It can be concluded from this plot that when the pH value is lower than 7, the reaction between GSH and Thioglo is relatively slow compared with solutions with higher pH value. Besides, there is a little decrease in the fluorescence intensity when pH value reaches 9. Possible reason is that at high pH value, GSH is oxidized quickly to GSSG.

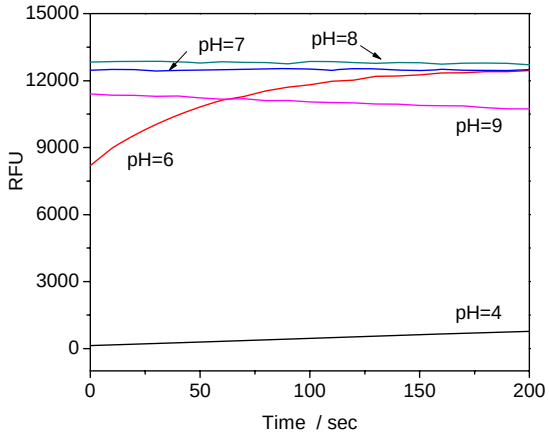

Figure 29. pH effect on the reaction between Thioglo 1 and GSH.

3.0 FUTURE WORK

3.1 ELECTROOSMOTIC SAMPLING

We are now developing a sampling method that uses electric fields to induce fluid flow in tissue while causing minimum damage to the cultures. This enables us to collect extracellular fluid from tissue for following analysis. Under an electric field, mobile counterions of fixed surface charges move, which creates fluid flow called electroosmosis. It is the most common driving force used in CE. The electroosmotic mobility is directly proportional to the zeta potential of the surface. Many literatures show that tissue will have a negative zeta potential.[143-149] It is this zeta potential that will motivate the flow of extracellular fluid out of tissue. Iontophoresis will further be combined with electroosmotic sampling, where perfusing solution can be pulled into tissue and an equivalent volume of fluid can be withdrawn without the need to apply pressure and without the need for a membrane.

3.2 GLUTATHIONE AND HIPPOCAMPUS

As mentioned before, astrocytes will release GSH under conditions and provides neurons with 'reducing power' that protects them. During this process, the GSH must first be broken down through hydrolysis by γ-glutamyltranspeptidase (γGT). Current techniques do not have the

time or spatial resolution to tease out the details of this process in organotypic hippocampal slice cultures. We will combine electroosmotic sampling with online derivatization (Thioglo-1) and separation (CE) to quantitate extracellular GSH levels and the release of GSH from astrocytes under certain conditions.

3.3 MICROFLUIDIC DEVICES AND OPERATION

The preliminary design of the microfluidic devices is similar to those mentioned in papers by Kennedy et al..[24, 150, 151] The sketch of the initial device is shown in Figure 30. An external power supply will provide a negative high voltage to the reservoir marked with "outlet". All other three channels will be connected to ground through electrodes. A ground-switch relay will control the gating sampling. A single sampling probe of about 10 cm, based on convenience, is in contact with the tissue culture. The other end of the capillary will be connected with the reservoir marked "sampling capillary inlet" through an Upchurch Nanoport. GSH collected from the culture by electroosmotic sampling will enter the system and meet the Thioglo 1 reagent supplied by the reagent channel, both of them will enter the reaction channel where mixing and reaction will be complete. After that the product is shunted to waste under the pressure provided by the gating channel. By changing the electric state of the gating reservoir to "float", a segment of the sample stream will be injected into the separation channel for analysis. A series of devices with different layout and length of the channels will be designed and compared for optimization of the system.

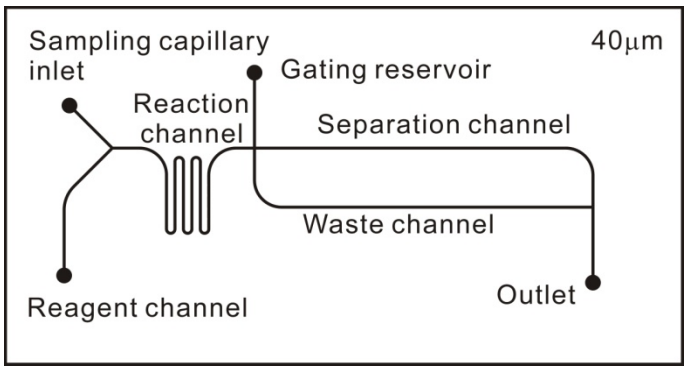

Figure 30. Sketch of the microfluidic device used in online detection.

BIBLIOGRAPHY

(1) Pastore, A.; Federici, G.; Bertini, E.; Piemonte, F. *Clinica Chimica Acta* **2003**, *333*, 19-39.
(2) Sies, H. *Free Radical Biology and Medicine* **1999**, *27*, 916-921.
(3) Camera, E.; Picardo, M. *Journal of Chromatography B-Analytical Technologies in the Biomedical and Life Sciences* **2002**, *781*, 181-206.
(4) Clark, D. D.; Sokoloff, L. In *Basic neurochemistry. Molecular, cellular and medical aspects,* 6 ed.; Siegel, G. J., Agranoff, B. W., Albers, R. W., Fisher, S. K., Uhler, M. D., Eds.; Lippincott-Raven: Philadelphia, 1999, pp 637-670.
(5) Dringen, R.; Hirrlinger, J. *Biological Chemistry* **2003**, *384*, 505-516.
(6) Dringen, R.; Gutterer, J. M.; Hirrlinger, J. *European Journal of Biochemistry* **2000**, *267*, 4912-4916.
(7) Dringen, R. *Progress in Neurobiology* **2000**, *62*, 649-671.
(8) Vina, J.; Sastre, J.; Asensi, M.; Packer, L. In *Biothiols, Pt A*; Academic Press Inc: San Diego, 1995; Vol. 251, pp 237-243.
(9) Liang, S. C.; Wang, H.; Zhang, Z. M.; Zhang, X.; Zhang, H. S. *Analytica Chimica Acta* **2002**, *451*, 211-219.
(10) Inoue, T.; Kirchhoff, J. R. *Analytical Chemistry* **2000**, *72*, 5755-5760.
(11) Inoue, T.; Kirchhoff, J. R. *Analytical Chemistry* **2003**, *75*, 4942-4942.
(12) Khramtsov, V. V.; Yelinova, V. I.; Glazachev, Y. I.; Reznikov, V. A.; Zimmer, G. *Journal of Biochemical and Biophysical Methods* **1997**, *35*, 115-128.
(13) Kuster, A.; Tea, I.; Sweeten, S.; Roze, J. C.; Robins, R. J.; Darmaun, D. *Analytical and Bioanalytical Chemistry* **2008**, *390*, 1403-1412.
(14) Lyons, J.; Rauh-Pfeiffer, A.; Yu, Y. M.; Lu, X. M.; Zurakowski, D.; Tompkins, R. G.; Ajami, A. M.; Young, V. R.; Castillo, L. *Proceedings of the National Academy of Sciences of the United States of America* **2000**, *97*, 5071-5076.
(15) Capitan, P.; Malmezat, T.; Breuille, D.; Obled, C. *Journal of Chromatography B* **1999**, *732*, 127-135.
(16) Sun, Y.; Yin, X. F.; Lu, M. *Chinese Journal of Analytical Chemistry* **2007**, *35*, 469-473.
(17) Sun, Y.; Yin, X. F. *Journal of Chromatography A* **2006**, *1117*, 228-233.
(18) Ling, Y. Y.; Yin, X. F.; Fang, Z. L. *Chemical Journal of Chinese Universities-Chinese* **2005**, *26*, 247-249.
(19) Xia, F. Q.; Jin, W. R.; Yin, X. F.; Fang, Z. L. *Journal of Chromatography A* **2005**, *1063*, 227-233.
(20) Khandurina, J.; Guttman, A. *Journal of Chromatography A* **2002**, *943*, 159-183.
(21) Li, P. C. H.; Harrison, D. J. *Analytical Chemistry* **1997**, *69*, 1564-1568.
(22) Colyer, C. L.; Tang, T.; Chiem, N.; Harrison, D. J. *Electrophoresis* **1997**, *18*, 1733-1741.

(23) Huynh, B. H.; Fogarty, B. A.; Nandi, P.; Lunte, S. A. *Journal of Pharmaceutical and Biomedical Analysis* **2006**, *42*, 529-534.
(24) Sandlin, Z. D.; Shou, M. S.; Shackman, J. G.; Kennedy, R. T. *Analytical Chemistry* **2005**, *77*, 7702-7708.
(25) Cellar, N. A.; Burns, S. T.; Meiners, J. C.; Chen, H.; Kennedy, R. T. *Analytical Chemistry* **2005**, *77*, 7067-7073.
(26) Garcia-Campana, A. M.; Taverna, M.; Fabre, H. *Electrophoresis* **2007**, *28*, 208-232.
(27) Johnson, M. E.; Landers, J. P. *Electrophoresis* **2004**, *25*, 3513-3527.
(28) Mogensen, K. B.; Klank, H.; Kutter, J. P. *Electrophoresis* **2004**, *25*, 3498-3512.
(29) Meister, A.; Anderson, M. E. *Annual Review of Biochemistry* **1983**, *52*, 711-760.
(30) Richman, P. G.; Meister, A. *The Journal of Biological chemistry* **1975**, *250*, 1422-1426.
(31) Wang, X. F.; Cynader, M. S. *Journal of Neurochemistry* **2000**, *74*, 1434-1442.
(32) Chen, Y. M.; Vartiainen, N. E.; Ying, W. H.; Chan, P. H.; Koistinaho, J.; Swanson, R. A. *Journal of Neurochemistry* **2001**, *77*, 1601-1610.
(33) Hertz, L.; Zielke, H. R. *Trends in Neurosciences* **2004**, *27*, 735-743.
(34) Kranich, O.; Dringen, R.; Sandberg, M.; Hamprecht, B. *Glia* **1998**, *22*, 11-18.
(35) Dringen, R.; Pfeiffer, B.; Hamprecht, B. *Journal of Neuroscience* **1999**, *19*, 562-569.
(36) Kranich, O.; Hamprecht, B.; Dringen, R. *Neuroscience Letters* **1996**, *219*, 211-214.
(37) Dringen, R.; Kussmaul, L.; Hamprecht, B. *Glia* **1998**, *23*, 139-145.
(38) Awasthi, Y. C.; Sharma, R.; Singhal, S. S. *International Journal of Biochemistry* **1994**, *26*, 295-308.
(39) Salinas, A. E.; Wong, M. G. *Current Medicinal Chemistry* **1999**, *6*, 279-309.
(40) Rushmore, T. H.; Pickett, C. B. *Journal of Biological Chemistry* **1993**, *268*, 11475-11478.
(41) Li, X. Y.; Orwar, O.; Revesjo, C.; Sandberg, M. *Neurochemistry International* **1996**, *29*, 121-128.
(42) Juurlink, B. H. J.; Schultke, E.; Hertz, L. *Brain Research* **1996**, *710*, 229-233.
(43) Sagara, J. I.; Makino, N.; Bannai, S. *Journal of Neurochemistry* **1996**, *66*, 1876-1881.
(44) Li, X. Y.; Wallin, C.; Weber, S. G.; Sandberg, M. *Brain Research* **1999**, *815*, 81-88.
(45) Hirrlinger, J.; Schulz, J. B.; Dringen, R. *Journal of Neurochemistry* **2002**, *82*, 458-467.
(46) Swanson, R. A.; Ying, W.; Kauppinen, T. M. *Current Molecular Medicine* **2004**, *4*, 193-205.
(47) Stridh, M. H.; Tranberg, M.; Weber, S. G.; Blomstrand, F.; Sandberg, M. *Journal of Biological Chemistry* **2008**, *283*, 10347-10356.
(48) Hirrlinger, J.; Schulz, J. B.; Dringen, R. *Journal of Neuroscience Research* **2002**, *69*, 318-326.
(49) Stewart, V. C.; Stone, R.; Gegg, M. E.; Sharpe, M. A.; Hurst, R. D.; Clark, J. B.; Heales, S. J. R. *Journal of Neurochemistry* **2002**, *83*, 984-991.
(50) Dringen, R.; Kranich, O.; Hamprecht, B. *Neurochemical Research* **1997**, *22*, 727-733.
(51) Devesa, A.; Oconnor, J. E.; Garcia, C.; Puertes, I. R.; Vina, J. R. *Brain Research* **1993**, *618*, 181-189.
(52) Sies, H.; Gerstenecker, C.; Menzel, H.; Flohé, L. *FEBS letters* **1972**, *27*, 171-175.
(53) Leier, I.; Jedlitschky, G.; Buchholz, U.; Center, M.; Cole, S. P. C.; Deeley, R. G.; Keppler, D. *Biochemical Journal* **1996**, *314*, 433-437.
(54) Bains, J. S.; Shaw, C. A. *Brain Research Reviews* **1997**, *25*, 335-358.
(55) Benzi, G.; Moretti, A. *Neurobiology of Aging* **1995**, *16*, 661-674.

(56) Do, K. Q.; Trabesinger, A. H.; Kirsten-Kruger, M.; Lauer, C. J.; Dydak, U.; Hell, D.; Holsboer, F.; Boesiger, P.; Cuenod, M. *European Journal of Neuroscience* **2000**, *12*, 3721-3728.
(57) Wilson, J. X. *Canadian Journal of Physiology and Pharmacology* **1997**, *75*, 1149-1163.
(58) Contestabile, A. *Expert Opinion on Therapeutic Patents* **2001**, *11*, 573-585.
(59) Slemmer, J. E.; Shacka, J. J.; Sweeney, M. I.; Weber, J. T. *Current Medicinal Chemistry* **2008**, *15*, 404-414.
(60) Meister, A. *Journal of Biological Chemistry* **1994**, *269*, 9397-9400.
(61) Rice, M. E.; Perezpinzon, M. A.; Lee, E. J. K. *Journal of Neurophysiology* **1994**, *71*, 1591-1596.
(62) Cooper, A. J. L.; Kristal, B. S. *Biological Chemistry* **1997**, *378*, 793-802.
(63) Cotgreave, I. A.; Gerdes, R. G. *Biochemical and Biophysical Research Communications* **1998**, *242*, 1-9.
(64) Moriarty-Craige, S. E.; Jones, D. P. *Annual Review of Nutrition* **2004**, *24*, 481-509.
(65) Shih, A. Y.; Erb, H.; Sun, X.; Toda, S.; Kalivas, P. W.; Murphy, T. H. *Journal of Neuroscience* **2006**, *26*, 10514-10523.
(66) Filomeni, G.; Aquilano, K.; Rotilio, G.; Ciriolo, M. R. *Cancer Research* **2005**, *65*, 11735-11742.
(67) Hall, A. G. In *Drug Resistance in Leukemia and Lymphoma*; Kaspers, G. J. L., Pieters, R., Veerman, A. J. P., Eds.; Kluwer Academic Publishers: Dordrecht, 1999; Vol. III, pp 199-203.
(68) Schafer, F. Q.; Buettner, G. R. *Free Radical Biology and Medicine* **2001**, *30*, 1191-1212.
(69) Orwar, O.; Li, X. Y.; Andine, P.; Bergstrom, C. M.; Hagberg, H.; Folestad, S.; Sandberg, M. *Journal of Neurochemistry* **1994**, *63*, 1371-1376.
(70) Yang, C. S.; Chou, S. T.; Lin, N. N.; Liu, L.; Tsai, P. J.; Kuo, J. S.; Lai, J. S. *Journal of Chromatography B-Biomedical Applications* **1994**, *661*, 231-235.
(71) Zangerle, L.; Cuenod, M.; Winterhalter, K. H.; Do, K. Q. *Journal of Neurochemistry* **1992**, *59*, 181-189.
(72) Guo, N.; McIntosh, C.; Shaw, C. *Neuroscience* **1992**, *51*, 835-842.
(73) Shaw, C. A.; Pasqualotto, B. A.; Curry, K. *Neuroreport* **1996**, *7*, 1149-1152.
(74) Janaky, R.; Ogita, K.; Pasqualotto, B. A.; Bains, J. S.; Oja, S. S.; Yoneda, Y.; Shaw, C. A. *Journal of Neurochemistry* **1999**, *73*, 889-902.
(75) Varga, V.; Jenei, Z.; Janaky, R.; Saransaari, P.; Oja, S. S. *Neurochemical Research* **1997**, *22*, 1165-1171.
(76) Ogita, K.; Enomoto, R.; Nakahara, F.; Ishitsubo, N.; Yoneda, Y. *Journal of Neurochemistry* **1995**, *64*, 1088-1096.
(77) Anderson, M. E.; Underwood, M.; Bridges, R. J.; Meister, A. *The FASEB Journal* **1989**, *3*, 2527-2531.
(78) Regan, R. F.; Guo, Y. P. *Brain Research* **1999**, *817*, 145-150.
(79) Regan, R. F.; Guo, Y. P. *Neuroscience* **1999**, *91*, 463-470.
(80) Senft, A. P.; Dalton, T. P.; Shertzer, H. G. *Analytical Biochemistry* **2000**, *280*, 80-86.
(81) Carru, C.; Deiana, L.; Sotgia, S.; Pes, G. M.; Zinellu, A. *Electrophoresis* **2004**, *25*, 882-889.
(82) Yoshida, T. *Journal of Chromatography B-Biomedical Applications* **1996**, *678*, 157-164.
(83) Hogan, B. L.; Yeung, E. S. *Analytical Chemistry* **1992**, *64*, 2841-2845.
(84) Gao, J.; Yin, X. F.; Fang, Z. L. *Lab on a Chip* **2004**, *4*, 47-52.

(85) Qin, J. H.; Ye, N. N.; Yu, L. F.; Liu, D. Y.; Fung, Y. S.; Wang, W.; Ma, X. J.; Lin, B. C. *Electrophoresis* **2005**, *26*, 1155-1162.
(86) Ling, Y. Y.; Yin, X. F.; Fang, Z. L. *Electrophoresis* **2005**, *26*, 4759-4766.
(87) Sakhi, A. K.; Blomhoff, R.; Gundersen, T. E. *Journal of Chromatography A* **2007**, *1142*, 178-184.
(88) Wallin, C.; Puka-Sundvall, M.; Hagberg, H.; Weber, S. G.; Sandberg, M. *Developmental Brain Research* **2000**, *125*, 51-60.
(89) Lenton, K. J.; Therriault, H.; Wagner, J. R. *Analytical Biochemistry* **1999**, *274*, 125-130.
(90) Nozal, M. J.; Bernal, J. L.; Toribio, L.; Marinero, P.; Moral, O.; Manzanas, L.; Rodriguez, E. *Journal of Chromatography A* **1997**, *778*, 347-353.
(91) Wallin, C.; Weber, S. G.; Sandberg, M. *Journal of Neurochemistry* **1999**, *73*, 1566-1572.
(92) Chaurasia, C. S.; Muller, M.; Bashaw, E. D.; Benfeldt, E.; Bolinder, J.; Bullock, R.; Bungay, P. M.; DeLange, E. C. M.; Derendorf, H.; Elmquist, W. F.; Hammarlund-Udenaes, M.; Joukhadar, C.; Kellogg, D. L.; Lunte, C. E.; Nordstrom, C. H.; Rollema, H.; Sawchuk, R. J.; Cheung, B. W. Y.; Shah, V. P.; Stahle, L.; Ungerstedt, U.; Welty, D. F.; Yeo, H. *Aaps Journal* **2007**, *9*, E48-E59.
(93) Lada, M. W.; Kennedy, R. T. *Journal of Neuroscience Methods* **1997**, *72*, 153-159.
(94) Han, J. L.; Cheng, F. C.; Yang, Z. L.; Dryhurst, G. *Journal of Neurochemistry* **1999**, *73*, 1683-1695.
(95) Shi, G. Y.; Lu, J. X.; Xu, F.; Sun, W. L.; Jin, L. T.; Yamamoto, K.; Tao, S. G.; Jin, J. Y. *Analytica Chimica Acta* **1999**, *391*, 307-313.
(96) Causse, E.; Issac, C.; Malatray, P.; Bayle, C.; Valdiguie, P.; Salvayre, R.; Couderc, F. *Journal of Chromatography A* **2000**, *895*, 173-178.
(97) Lada, M. W.; Kennedy, R. T. *Journal of Neuroscience Methods* **1995**, *63*, 147-152.
(98) Tietze, F. *Analytical Biochemistry* **1969**, *27*, 502-522.
(99) Trabesinger, A. H.; Boesiger, P. *Magnetic Resonance in Medicine* **2001**, *45*, 708-710.
(100) Trabesinger, A. H.; Weber, O. M.; Duc, C. O.; Boesiger, P. *Magnetic Resonance in Medicine* **1999**, *42*, 283-289.
(101) Kennett, E. C.; Bubb, W. A.; Bansal, P.; Alewood, P.; Kuchel, P. W. *Redox Report* **2005**, *10*, 83-90.
(102) Manz, A.; Grabera, N.; Widmera, H. M. *Sensors and Actuators B-Chemical* **1990**, *1*, 244-248.
(103) Tabeling, P. *Introduction to microfluidics* Oxford University Press: New York, 2005.
(104) Manza, A.; Grabera, N.; Widmera, H. M. *Sensors and Actuators B-Chemical* **1990**, *1*, 244-248.
(105) Reyes, D. R.; Iossifidis, D.; Auroux, P. A.; Manz, A. *Analytical Chemistry* **2002**, *74*, 2623-2636.
(106) Auroux, P. A.; Iossifidis, D.; Reyes, D. R.; Manz, A. *Analytical Chemistry* **2002**, *74*, 2637-2652.
(107) Vilkner, T.; Janasek, D.; Manz, A. *Analytical Chemistry* **2004**, *76*, 3373-3385.
(108) Dittrich, P. S.; Tachikawa, K.; Manz, A. *Analytical Chemistry* **2006**, *78*, 3887-3907.
(109) Chen, X. G.; Fan, L. Y.; Hu, Z. *Electrophoresis* **2004**, *25*, 3962-3969.
(110) Karger, B. L.; Snyder, L. R.; Horvath, C. *An introduction to separation science*; John Wiley & Sons, Inc: New York, 1973.
(111) Probstein, R. F. *Physicochemical hydrodynamics: an introduction, 2nd Ed.*; John Wiley & Sons, Inc: New York, 1994.

(112) Manz, A.; Harrison, D. J.; Verpoorte, E.; Widmer, H. M. *Advances in Chromatography* **1993**, *33*, 1-66.
(113) Skoog, D. A.; Holler, F. J.; Nieman, T. A. *Principles of Instrumental Analysis, 5th Ed.*; Saunders college Publishing: Philadelphia, 1998.
(114) Bruus, H. *Theoretical microfluidics*; Oxford University Press: New York, 2008.
(115) Uchiyama, K.; Nakajima, H.; Hobo, T. *Analytical and Bioanalytical Chemistry* **2004**, *379*, 375-382.
(116) Nicholson, C.; Tao, L. *Biophysical Journal* **1993**, *65*, 2277-2290.
(117) GASSMANN, E.; KUO, J. E.; ZARE, R. N. *Science* **1985**, *230*, 813 - 814.
(118) Cheng, Y.-f.; Dovichi, N. J. *Science* **1988**, *242*, 562-564.
(119) Wu, S. L.; Dovichi, N. J. *Journal of Chromatography* **1989**, *480*, 141-155.
(120) Peck, K.; Stryer, L.; Glazer, A. N.; Mathies, R. A. *Proc. Natl. Acad. Sci. USA* **1989**, *86*, 4087-4091.
(121) Mathies, R. A.; Peck, K.; Stryer, L. *analytical Chemistry* **1990**, *62*, 1786-1791.
(122) Hernandez, L.; Escalona, J.; Joshi, N.; Guzman, N. *Journal of Chromatography A* **1991**, *559*, 183-196.
(123) Legendre, B. L.; Moberg, D. L.; Williams, D. C.; Soper, S. A. *Journal of Chromatography A* **1997**, *779*, 185-194.
(124) Jiang, G. F.; Attiya, S.; Ocvirk, G.; Lee, W. E.; Harrison, D. J. *Biosensors & Bioelectronics* **2000**, *14*, 861-869.
(125) Gotz, S.; Karst, U. *Sensors and Actuators B-Chemical* **2007**, *123*, 622-627.
(126) Ocvirk, G.; Tang, T.; Harrison, D. J. *Analyst* **1998**, *123*, 1429-1434.
(127) Fu, J. L.; Fang, Q.; Zhang, T.; Jin, X. H.; Fang, Z. L. *Analytical Chemistry* **2006**, *78*, 3827-3834.
(128) Hellmich, W.; Greif, D.; Pelargus, C.; Anselmetti, D.; Ros, A. *Journal of Chromatography A* **2006**, *1130*, 195-200.
(129) Pasas, S. A.; Lacher, N. A.; Davies, M. I.; Lunte, S. M. *Electrophoresis* **2002**, *23*, 759-766.
(130) Long, Z. C.; Liu, D. Y.; Ye, N. N.; Qin, J. H.; Lin, B. C. *Electrophoresis* **2006**, *27*, 4927-4934.
(131) Gao, N.; Li, L.; Shi, Z. K.; Zhang, X. L.; Jin, W. R. *Electrophoresis* **2007**, *28*, 3966-3975.
(132) Miyaki, K.; Zeng, H. L.; Nakagama, T.; Uchiyama, K. *Journal of Chromatography A* **2007**, *1166*, 201-206.
(133) Kawazumi, H.; Song, J. M.; Inoue, T.; Ogawa, T. *Analytical Sciences* **1995**, *11*, 587-590.
(134) Owens, C. V.; Davidson, Y. Y.; Kar, S.; Soper, S. A. *Analytical Chemistry* **1997**, *69*, 1256-1261.
(135) Guttman, A.; Ronai, Z.; Barta, C.; Hou, Y. M.; Sasvari-Szekely, M.; Wang, X.; Briggs, S. P. *Electrophoresis* **2002**, *23*, 1524-1530.
(136) Lu, Q.; Collins, G. E. *Analyst* **2001**, *126*, 429-432.
(137) Yan, Q.; Chen, R. S.; Cheng, J. K. *Analytica Chimica Acta* **2006**, *555*, 246-249.
(138) Ingle, J. D. J.; Crouch, S. R. *Spectrochemcial analysis*; Prentice Hall, Inc.: Upper Saddle River, 1988.
(139) Kaufmann, K. In *OE Magazine*, 2005.
(140) In *Melles Griot Catolog: the practical application of light*; Vol. x.
(141) Self, S. A. *Applied Optics* **1983**, *22*, 658-661.
(142) Morgan, D. M.; Weber, S. G. *analytical Chemistry* **1984** *56*, 2560-2567.

(143) Vijh, A. K. *Journal of Materials Science: Materials in Medicine* **1999**, *10*, 419-423.
(144) Walsh, W. R.; Guzelsu, N. *Biomaterials* **1993**, *14*, 331-336.
(145) Van Wagenen, R. A.; Andrade, J. D.; Hibbs, J. B., Jr. *J. Electrochem. Soc.* **1976**, *123*, 1438-1444.
(146) Miyake, M.; Kurihara, K. *Biochim. Biophys. Acta* **1983**, *762*, 256-264.
(147) Nilsson, B. O.; Hjerten, S. *Biol. Reprod.* **1982**, *27*, 485-493.
(148) Brewer, G. J. *J. Theor. Biol.* **1980**, *85*, 75-82.
(149) Badrakhan, C. D.; Petrat, F.; Holzhauser, M.; Fuchs, A.; Lomonosova, E. E.; de Groot, H.; Kirsch, M. *Journal of Biochemical and Biophysical Methods* **2004**, *58*, 207-218.
(150) Roper, M. G.; Shackman, J. G.; Dahlgren, G. M.; Kennedy, R. T. *Analytical Chemistry* **2003**, *75*, 4711-4717.
(151) Shackman, J. G.; Dahlgren, G. M.; Peters, J. L.; Kennedy, R. T. *Lab on a Chip* **2005**, *5*, 56-63.